Journal of Catalysis 368 (2018) 261–274

Contents lists available at ScienceDirect

Journal of Catalysis

journal homepage: www.elsevier.com/locate/jcat

Direct synthesis of H_2O_2 on PdZn nanoparticles: The impact of electronic modifications and heterogeneity of active sites

Neil M. Wilson [a], Johanna Schröder [b], Pranjali Priyadarshini [a], Daniel T. Bregante [a], Sebastian Kunz [b], David W. Flaherty [a,*]

[a] Department of Chemical and Biomolecular Engineering, University of Illinois Urbana-Champaign, Urbana, IL 61801, United States
[b] Institute of Applied and Physical Chemistry, University of Bremen, Bremen, Germany

ARTICLE INFO

Article history:
Received 5 June 2018
Revised 10 September 2018
Accepted 17 September 2018

Keywords:
Hydrogen peroxide
Intermetallics
Catalyst uniformity
Mechanism
Electronic effects
Proton electron transfer

ABSTRACT

The direct synthesis of H_2O_2 ($H_2 + O_2 \rightarrow H_2O_2$) would reduce the cost of H_2O_2, but few catalytic materials demonstrably provide the necessary combination of high H_2O_2 selectivity and stability over long periods of continuous reaction. Here, we show that silica supported $PdZn_x$ nanoparticles (where x indicates the bulk composition, $0 \leq x \leq 30$) are stable and selective catalysts for the continuous production of H_2O_2 in the absence of liquid-phase promoters. Increasing the ratio of Zn to Pd precursors in the synthesis lead to distributions of nanoparticles that contain greater fractions of β_1-Pd_1Zn_1 and lower fractions of face-centered cubic (fcc) Pd nanoparticles. A combination of the measured functional dependence of steady-state H_2O_2 and H_2O formation rates on H_2 and O_2 pressures and the need for protic solvents indicate that H_2O_2 forms on all members of the $PdZn_x$ series by proton-electron transfer steps to dioxygen and hydroperoxy surface intermediates that saturate active sites during catalysis. Primary H_2O_2 selectivities increase systematically with the Zn to Pd ratio and range from 26% on fcc Pd nanoparticles to 69% on $PdZn_{30}$ catalysts, which contains β_1-Pd_1Zn_1 nanoparticles and lacks detectable amounts of fcc Pd. The differences in H_2O_2 selectivities among the $PdZn_x$ catalysts reflect changes in activation enthalpies ($\Delta H^{\ddagger}$) for H_2O_2 (from -3 to 14 kJ mol^{-1}) and H_2O (11 to 44 kJ mol^{-1}) formation. These results demonstrate that pathways for H_2O_2 formation are less sensitive than H_2O formation to electronic differences between active sites on fcc Pd and intermetallic β_1-Pd_1Zn_1 nanoparticles, whose densities of states differ significantly near the Fermi level. Comparisons of the ratios of H_2O_2 and H_2O formation rates to $\Delta H^{\ddagger}$ values among Pd and $PdZn_x$ catalysts show that the increases in H_2O_2 selectivities are less than predicted from the differences in $\Delta H^{\ddagger}$ values alone. This analysis shows that the current synthesis method introduces at least two distinguishable catalytically active sites, and a portion of the sites formed predominantly cleave O-O bonds in primary and secondary reaction pathways that form H_2O and lead to lower H_2O_2 selectivities than would be achieved in their absence. These findings demonstrate that differences in electronic structure of active sites cause β-Pd_1Zn_1 nanoparticles to give greater H_2O_2 selectivities than Pd catalysts and suggest that a synthesis procedure that uniformly creates β-Pd_1Zn_1 and alloys all Pd on the support may lead to increasingly selective conversion of O_2 and H_2 to H_2O_2.

1. Introduction

The direct synthesis of H_2O_2 from molecular hydrogen and oxygen ($H_2 + O_2 \rightarrow H_2O_2$) is a promising alternative to the industrial standard for H_2O_2 production, the Riedl-Pfleiderer (RP) process (i.e., the auto-oxidation of anthraquinones) [1]. The RP process requires significant infrastructure and energy for separations to generate 30–70 wt.% solutions of H_2O_2 that are transported to the point of use [2]. Coupling RP with an oxidation process on site, such as the epoxidation of propylene within the hydrogen peroxide propylene oxide (HPPO) process [3,4], results in a significant decrease in energy usage (35%) [5]. Ultimately, this reduces the expense and environmental impact of H_2O_2 produced by the RP process, because H_2O_2 is produced on site, reducing concentration and transportation costs. However RP chemistry is only operated at large scales ($\sim 2 \times 10^5$ tons H_2O_2 year^{-1}) due to significant capital expenditures [6]. As such, the RP process couples well only with other processes of similar scale, such as PO production [7]. Other oxidative processes like pulp and paper bleaching [8] and

* Corresponding author.
E-mail address: dwflhrty@illinois.edu (D.W. Flaherty).

https://doi.org/10.1016/j.jcat.2018.09.020
0021-9517/

wastewater treatment [9] utilize less benign oxidants (e.g., HOCl, Cl_2) [8,10] due, in part, to the cost of constructing RP facilities.

The direct synthesis of H_2O_2 has a key advantage over the RP process: direct synthesis of H_2O_2 could be implemented with less expense and at smaller scales [11]. The direct synthesis reaction proceeds in a single reactor in water or aqueous alcohol solvents, which eliminates the need for many of the unit operations required in the reactor and separation trains used with anthraquinone oxidation chemistry. This difference results in less infrastructure but also lower energy consumption in comparison to the RP process [11]. Unfortunately, the thermodynamically preferred product of direct synthesis on supported transition metal catalysts (e.g., Pd) is H_2O [12–14]. There are clear benefits to using direct synthesis over RP, and as such significant research has been conducted on developing catalysts which can achieve H_2O_2 selectivities comparable to RP (>95%) [15].

Recent work has improved our understanding of the mechanism for the direct synthesis of H_2O_2 and informs molecular interpretations of strategies used to increase selectivities and rates of this reaction [16]. Alloying Pd with various transition metals (e.g., Au [14,17–19], Sn [20], Zn [20,21], Pt [22,23]) increases H_2O_2 selectivities and has several advantages over alternative approaches that involve adding mineral acids (e.g., H_2SO_4 [17], HCl [24,25], HBr [12,17,26,27], H_3PO_4 [13,27]) or halide salts (e.g., KCl [12], NaBr [13,28]) to the solvent. These liquid-phase promoters improve H_2O_2 selectivities but the effect of these additives on catalysts and reactions that utilize H_2O_2 downstream are not well understood. Bimetallic catalysts can provide comparable H_2O_2 selectivities to those obtained through the addition of halide modifiers (e.g., AuPd [13] and PdSn [20] provide >95% H_2O_2 selectivity; while Pd in aqueous solutions with 0.1 M HCl and 0.01 M NaBr gives ~95% H_2O_2 [26]), however, Pd oxidizes and dissolves from the support at the concentrations of halides often used in published studies. As a result, significant H_2O_2 direct synthesis research has been directed towards bimetallic catalysts. Since the initial discovery that AuPd is a selective H_2O_2 direct synthesis catalyst in 2003 [17], AuPd has been shown many times to be the benchmark bimetallic direct synthesis catalyst, which can obtain H_2O_2 selectivities and formation rates as high as 98% and $6.4{\cdot}10^3$ mol H_2O_2 kg_{Pd}^{-1} h^{-1}, respectively [13]. In comparison, Pd catalyst in the same system only achieves an H_2O_2 selectivity of 42% and a H_2O_2 formation rate of $1.0{\cdot}10^3$ mol H_2O_2 kg_{Pd}^{-1} h^{-1} [13]. Recently, H_2O_2 selectivities and formation rates as high as 96% and $6.1{\cdot}10^3$ mol H_2O_2 kg_{Pd}^{-1} h^{-1} have been obtained in a semi-batch reactor using titania supported PdSn catalyst prepared by incipient wetness impregnation and pretreated using alternating reduction and oxidation steps [20]. Hutchings and coworkers demonstrated also that when alloyed with Pd, metals other than Sn (e.g., Ni, Zn, Ga, In, Co) can eliminate secondary reactions which decompose H_2O_2 and obtain H_2O_2 formation rates between $3.0{\cdot}10^3$ and $6.4{\cdot}10^3$ mol H_2O_2 kg_{Pd}^{-1} h^{-1} [20]. Work by Zhang et al. has shown PdZn to be a selective direct synthesis catalyst as well (79% H_2O_2 in a semi-batch reactor in acidified ethanol, 0.03 M H_2SO_4) [21]. Collectively, these findings indicate that alloying Pd with metals other than Au can result in high H_2O_2 selectivity. Yet the reasons for these selectivity improvements, which may be caused by mechanistic, energetic, or other differences, have not been shown in previous investigations. We have recently provided evidence that AuPd catalysts have higher H_2O_2 selectivities than Pd, primarily because Au electronically modifies the Pd active sites likely by hybridization of intra-atomic orbitals that affects the d-band structure of Pd [29]. Such insight provides guidance for the synthesis of increasingly selective and productive catalysts, and consequently, detailed mechanistic and kinetic investigations of this chemistry should be used to understand emerging Pd bimetallic catalysts (e.g., PdSn, PdZn, etc.).

In this work, we measure steady-state H_2O_2 and H_2O formation rates and H_2O_2 hydrogenation rates in a plug-flow reactor on silica-supported Pd and $PdZn_x$ (where x denotes the bulk molar ratio of Zn to Pd) nanoparticles between 7 and 26 nm in diameter. These data, combined with semi-batch measurements in protic and aprotic solvents, show that direct synthesis on all $PdZn_x$ nanoparticles involves proton-electron transfer (PET) steps that reduce chemisorbed O_2, as reported for Pd [30], AuPd [29], and AgPt [31]. Increasing the bulk ratio of Zn to Pd to produce bulks compositions from Pd to $PdZn_{30}$ results in a concomitant increase in H_2O_2 selectivities from 26 to 69% in the absence of acid or halide promoters. Comparisons of H_2O_2 selectivities to X-ray diffractograms of the Pd and $PdZn_x$ samples suggests that these selectivity differences result primarily from a change in the ratio of nanoparticles with the β_1-Pd_1Zn_1 phase to those with the face-centered cubic (fcc) structure of Pd within the catalyst, rather than an increase in the ratio of Zn to Pd within individual nanoparticles. Values of the apparent activation enthalpies for H_2O_2 ($\Delta H^{\ddagger}_{H_2O_2}$) and H_2O ($\Delta H^{\ddagger}_{H_2O}$) formation show that increasing the ratio of β_1-Pd_1Zn_1 to fcc Pd nanoparticles in a given sample results in significant increases in the values of $\Delta H^{\ddagger}_{H_2O_2}$ and $\Delta H^{\ddagger}_{H_2O}$ (from −3 to 14 kJ mol^{-1} and from 11 to 44 kJ mol^{-1}, respectively). In the context of the catalytic cycle, these differences imply that active sites exposed on β_1-Pd_1Zn_1 nanoparticles possess lower densities of occupied states near the Fermi level in comparison to sites on Pd nanoparticles, which is consistent with comparisons of the calculated and measured electronic structures of these materials [32–35]. The combined results of this work show that electronic differences between the active sites on β_1-Pd_1Zn_1 and those of Pd contribute to greater H_2O_2 selectivities and that the highest H_2O_2 selectivities correspond to catalyst compositions that contain a sufficient amount of Zn to suppress the formation of fcc Pd nanoparticles during synthesis. Yet, catalysts containing all Pd atoms in the form of β_1-Pd_1Zn_1 nanoparticles give H_2O_2 selectivities much lower than expected from the large differences between activation enthalpies for H_2O and H_2O_2 formation (i.e., $\Delta H^{\ddagger}_{H_2O}$-$\Delta H^{\ddagger}_{H_2O_2}$ = 30 kJ mol^{-1}). This disparity indicates that a large number of distinct active sites with low barriers for O-O bond dissociation exist on the catalyst support, and these sites likely originate from consequential but small amounts of stray oligomeric or atomic Pd (<1 nm) that do not alloy with Zn. These findings provide insight into why $PdZn_x$ materials effectively catalyze direct synthesis and offer guidance to further increase H_2O_2 selectivities on similar $PdZn_x$ materials.

2. Methods and materials characterization

2.1. Synthesis of Pd and $PdZn_x$ nanoparticles supported on silica

The procedure used here for synthesizing silica supported $PdZn_x$ nanoparticles was inspired by a procedure for creating PdSn-SnO_2 [36]. The synthesis procedure for the Pd_1Zn_{30} catalysts is described in detail below, and other Pd:Zn metal ratios and metal loadings were synthesized by adjusting the ratio of Pd and Zn metal precursors used or the amount of silica added to the synthesis vessel. To begin, 420 mg of $ZnCl_2$ (Sigma-Aldrich, ≥98%) was added to 75 cm^3 of ethylene glycol (EG; Fisher Scientific, ≥99.8%), and the solution was stirred at 600 rpm at ambient temperature (Thermo Scientific, Super-Nuova). Next, 68 mg of $PdCl_2$ (Sigma-Aldrich, ≥99.9%) was dissolved in 2 cm^3 of HCl (Macron, 36.5–38%), which became orange in color once the $PdCl_2$ fully dissolved. The $PdCl_2$-HCl solution was added to the stirring $ZnCl_2$-EG mixture along with 10 g of SiO_2 (Davisil 646, 300 m^2 g^{-1}, 35–60 mesh). Subsequently, 0.5 M NaOH (Sigma-Aldrich, ≥97%) in EG was added in 5 cm^3 intervals until the solution pH was between 9 and 10. The slurry was then heated to 433 K while stirring at 600 rpm. During this process,

the color of the solution changed from orange to black, which signifies the reduction of the metal cations to nanoparticles. The solution was held at 433 K for 2 h to ensure complete reduction of the metal cations. The solids were recovered by vacuum filtration and rinsed with ~600 cm^3 of deionized (DI) H_2O (17.8 MΩ · cm). The solids were dried for ~12 h at ambient temperature before heating to 673 K at 3 K min^{-1} under flowing H_2 and He (40 kPa H_2, 61 kPa He, 150 cm^3 min^{-1}). All gases used were from Airgas and were 99.999% pure unless otherwise stated. The catalyst was held at 673 K for 4 h with the intent to reduce any remaining oxidized metal and to remove excess H_2O.

Silica supported Pd catalysts were prepared using strong electrostatic adsorption (SEA) as described previously [30,37]. Briefly, 15 g of SiO_2 (Davisil 646, 300 m^2 g^{-1}, 35–60 mesh) was added to a basic (pH ≥ 11) aqueous solution containing NH_4OH (Macron 28–30 wt.%). Next, 17.4 mg of $Pd(NH_3)_4Cl_2$ (Sigma-Aldrich, ≥99.99%) was added to the basic solution, which was stirred by hand approximately every 0.5 h for 3 h. The solids were recovered by vacuum filtration and rinsed with ~500 cm^3 of DI H_2O before being allowed to dry at ambient temperature for ~12 h. The solid catalyst was then heated to 573 K at 3 K min^{-1} and held at 573 K for 4 h in H_2 and He (40 kPa H_2, 61 kPa He, 100 cm^3 min^{-1}). In order to increase the average diameter of the Pd nanoparticles, the catalyst was then heated to 973 K at 3 K min^{-1} and held at 973 K for 4 h in flowing dry air (100 cm^3 min^{-1}). A subsequent reduction procedure was conducted at 573 K for 4 h with a mixture of H_2 and He (40 kPa H_2, 61 kPa He, 100 cm^3 min^{-1}). A silica supported Zn catalyst (0.05 wt.% Zn) was prepared using SEA of $ZnCl_2$ (Sigma-Aldrich, >98%) within an aqueous solution of NH_4OH, analogous to the method used to deposit Pd onto silica. The rinsed, dry solids were heated to 673 K at 3 K min^{-1} and held at 673 K for 4 h in H_2 and He (40 kPa H_2, 61 kPa He, 150 cm^3 min^{-1}) with the intent to form Zn and ZnO domains reminiscent of those produced during the preparation of supported $PdZn_x$ nanoparticles.

The metal loading of the $PdZn_x$ catalysts synthesized for kinetic experiments were kept low (~0.05 wt.% Pd) in order to safely avoid mass transport limitations (Supporting Information, Section S1). Higher metal loadings (0.19–1.4 wt.% Pd) are needed to generate X-ray diffraction patterns used to characterize the structure of the ensemble of nanoparticles (Section 2.2.3). Therefore, higher

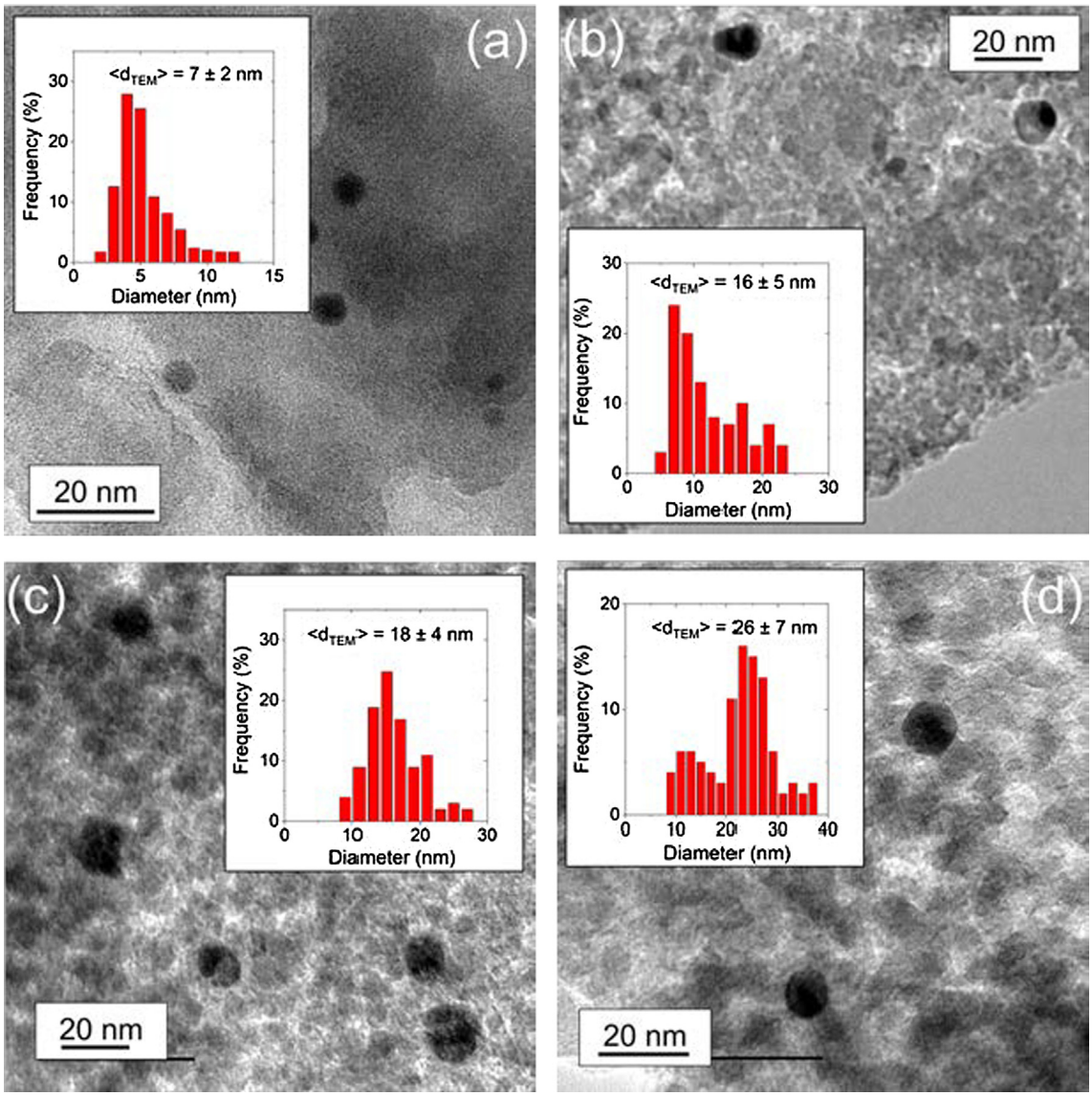

Fig. 1. Representative TEM images of low metal loading (0.04–0.05 wt.% Pd), silica-supported (a) Pd, (b) $PdZn_{1.5}$, (c) $PdZn_6$, and (d) $PdZn_{30}$ catalysts with their corresponding size distribution and $\langle d_{TEM} \rangle$ value as inset. >100 nanoparticles were counted for each size distribution.

metal loading Pd and $PdZn_x$ catalysts were prepared using SEA and EG reduction, respectively, according to the procedures described previously (higher metal loading catalysts are denoted by with ω; e.g., ω-Pd_1Zn_{20}). However, the amount of Pd precursor used for SEA and the number of $PdZn_x$ nanoparticles deposited onto the silica were increased to obtain the desired metal loading. As discussed below, transmission electron microscopy (TEM) images (Figs. 1 and S1) and selected area electron diffraction (SAED) patterns (Section S3) results show that the mean diameters and the phase of nanoparticles were similar between Pd and $PdZn_x$ samples with similar ratios of Zn to Pd but with different total metal content.

2.2. Compositional and structural characterization of Pd and $PdZn_x$ materials

2.2.1. Energy dispersive X-ray fluorescence spectroscopy

The metal content of each silica supported sample was determined using energy dispersive X-ray fluorescence (EDXRF) spectroscopy. Briefly, ~30 mg of each catalyst was finely ground and loaded into a polypropylene sample holder (1 cm diameter) that was sealed with ultralene film. These were then loaded into a spectrometer (Shimadzu, EDX-7000), whose sample chamber compartment was purged with He, and fluorescence spectra (0–30 keV) were used to calculate the mass percent of each element, shown in Table 1.

2.2.2. Transmission electron microscopy and selected area diffraction

Bright field TEM (JEOL 2010 LaB_6) was used to determine the distribution of nanoparticle diameters of the Pd and $PdZn_x$ catalysts. The catalysts were first ground to a fine powder (<200 mesh) and then dispersed onto Cu holey-carbon TEM grids (200 mesh, Ted Pella Inc.). After imaging the particles, the surface area normalized diameter ($\langle d_{TEM}\rangle$) was determined using:

$$\langle d_{TEM}\rangle = \frac{\sum_i n_i {d_i}^3}{\sum_i n_i {d_i}^2} \quad (1)$$

where n_i is the number of clusters with diameter d_i. Fig. 1 shows representative TEM images of the Pd and $PdZn_x$ catalysts used for kinetic measurements with their size distribution as an inset. All measured values of $\langle d_{TEM}\rangle$ are reported in Table 1. The values of $\langle d_{TEM}\rangle$ and their dispersion were higher on $PdZn_x$ catalysts than on the pure Pd catalysts, however, the mean diameters of all nanoparticles tested were sufficiently large such that their surfaces predominantly expose highly coordinated atoms contained within terraces [38].

Electron diffraction from individual nanoparticles in catalyst with low loadings revealed the presence of features indicative of fcc Pd in the Pd, $PdZn_{1.5}$ and $PdZn_6$ catalysts but also β_1-Pd_1Zn_1 domains in the samples containing Zn (Supporting Information, Section S3). Intensity profiles taken from diffractograms of the pure 0.05 wt.% Pd sample show reflections from the (1 1 1) and (2 0 0) planes of fcc Pd (Fig. S2). Reflections indicative of these same fcc Pd planes were found also in a significant fraction of the nanoparticles within the $PdZn_{1.5}$ (Figs. S3a and S3b) and $PdZn_6$ (Figs. S4a and S4b) materials. Yet these materials and $PdZn_{30}$ contained also a considerable number of nanoparticles that produced more closely spaced diffraction features corresponding to β_1-Pd_1Zn_1 nanoparticles (Figs. S3 and S4), based on previous syntheses [39–41] and XRD results (Section 2.2.3). These analyses of SAED patterns of multiple regions indicate that $PdZn_{1.5}$ and $PdZn_6$ materials contain a combination of both fcc Pd and β_1-Pd_1Zn_1 nanoparticles.

The $PdZn_{30}$ material was also characterized by dark-field scanning transmission electron microscopy (STEM; JEOL 2010F EF-FEG) in combination with energy dispersive X-ray spectroscopy (EDX; Oxford Instruments, 6498). Section S4 and Figs. S5a-e provide representative images and elemental maps derived from EDX. This analysis shows that Pd and Zn coexist within individual nanoparticles but also show extremely small quantities (near the detection limit, and undetectable by XRD) of Pd and Zn exist on the support as monometallic oligomers (<1 nm in diameter) despite the colloidal approach used to synthesize these catalysts. The heterogeneity of the Pd within these $PdZn_x$ catalysts was further examined by X-ray diffraction of analogous $PdZn_x$ materials with a higher metal loading.

2.2.3. X-ray diffraction

X-ray diffraction (XRD) was used to determine the bulk crystal structure of the nanoparticles within each catalyst. X-ray diffractograms were obtained using a diffractometer (Siemens/Bruker, D5000) with Cu Kα radiation (0.15418 nm) under ambient conditions. Both the low metal loading and the high metal loading (Section 2.2.1) catalysts were measured using XRD. Notably, the Pd, $PdZn_{1.5}$, and $PdZn_6$ catalysts did not yield observable diffraction features. Fig. 2 shows the measured XRD patterns for Pd and $PdZn_x$ catalysts which had detectable diffraction features. Known diffractograms were used to determine the identity of fcc Pd (i.e., (1 1 1) and (2 0 0) reflections at 2θ equal to 40 and 47 degrees. respectively) and β_1-Pd_1Zn_1 (i.e., (1 1 1) and (2 0 0) features at 2θ equal to 41 and 44 degrees, respectively) phases [39–41]. The only detectable phases of PdZn alloys were fcc $PdZn_y$ (where $y < 0.2$) and β_1-Pd_1Zn_1, the formation of which is consistent with

Table 1
Characterization results for Pd and $PdZn_x$ Catalysts.

Catalyst	Zn content (wt. %)[a]	Pd content (wt. %) [a]	Measured Zn:Pd Atomic Ratio	Temperature (K)		$\langle d_{TEM}\rangle$ [d] (nm)	Phases detected by XRD
				Oxidative treatment[b]	Reductive treatment[c]		
Pd	0	0.05	0	973, 4 h	573, 4 h	7 ± 2	nd[e]
$PdZn_{1.5}$	0.04	0.04	1.4	n/a	673, 4 h	16 ± 5	nd[e]
$PdZn_6$	0.14	0.04	5.8	n/a	673, 4 h	18 ± 4	nd[e]
$PdZn_{30}$	0.95	0.05	30	n/a	673, 4 h	26 ± 7	β_1-Pd_1Zn_1
ω-Pd	0	1.4	0	n/a	573, 4 h	27 ± 8	fcc Pd
ω-$PdZn_4$	0.85	0.35	4.0	n/a	673, 4 h	24 ± 6	fcc Pd, β_1-Pd_1Zn_1
ω-$PdZn_{20}$	2.2	0.19	20	n/a	673, 4 h	19 ± 5	β_1-Pd_1Zn_1

[a] Metal content determined by EDXRF.
[b] 100 cm^3 min^{-1} dry air.
[c] 40 kPa H_2, 61 kPa He, 100 cm^3 min^{-1}.
[d] Surface-averaged mean cluster diameter from TEM analysis from at least 100 clusters using Eq. (1).
[e] None detected.

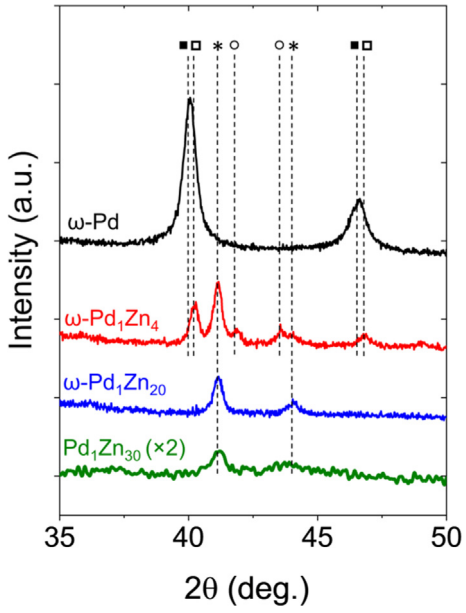

Fig. 2. X-Ray diffractograms for ω-Pd, ω-$PdZn_4$, ω-$PdZn_{20}$, and $PdZn_{30}$ materials. Diffraction features correspond to face centered cubic Pd (■), face centered cubic $PdZn_y$ (□, where y < 0.2), β_1-Pd_1Zn_1 (*), and unidentified phase (○), which is likely an oxide.

calculations that show spontaneous alloy formation for PdZn films on Pd(1 1 1) [42]. The ω-$PdZn_4$ catalyst contained a combination of diffraction peaks that shows the presence of both fcc $PdZn_y$ nanoparticles (shifted to higher 2θ values due to lattice contraction for $PdZn_y$ compared to Pd) and β_1-Pd_1Zn_1 nanoparticles within the same sample. Neither Zn nor ZnO were observed by XRD for any of the materials, although the composition of the materials indicates clearly that Zn from the synthesis exists within the catalyst at concentrations in excess of the Pd_1Zn_1 stoichiometry of the nanoparticles detected. Diffraction features (SAED and XRD) from catalysts with a significant molar excess of Zn relative to Pd (e.g., ω-$PdZn_{20}$ and $PdZn_{30}$) do not show detectable features that correspond to fcc Pd or $PdZn_y$ nanoparticles. These trends imply also that $PdZn_{1.5}$ and $PdZn_6$ materials contain mixtures of nanoparticles with fcc Pd, fcc $PdZn_y$, and β_1-Pd_1Zn_1 phases, however, the metal loadings of these catalysts are too low to detect crystal structures by XRD.

2.2.4. Temperature programmed reduction

Temperature programmed reduction (TPR) profiles were measured on Pd and $PdZn_x$ catalysts used for the kinetic measurements to confirm Pd and Zn were in contact within the $PdZn_x$ catalysts and to ensure that the catalysts would be reduced at the reduction pretreatments implemented (673 K, Section 2.1). Catalysts (700 mg) were loaded into a fused quartz tube (12 mm outer diameter, 10 mm inner diameter, 38 cm long) containing a quartz frit to support the catalyst. A thermocouple (Omega, type K) was located within an indentation in the outer wall of the quartz tube in close proximity to the catalyst bed, and the thermocouple was connected to a temperature controller (Watlow, EZ-ZONE PM) which was used to control a furnace (Lindberg, Hevi-Duty) surrounding the quartz tube and the catalyst. Digital mass flow controllers (MFC; Porter, series 601) were used to introduce combinations of He, H_2, and air cleaned of hydrocarbons (Parker, 76-830 Zero Air Generator) at known flowrates through a gas manifold (equipped with a reactor bypass) to the catalyst. The composition of the effluent gas was determined using a quadrupole mass spectrometer (QMS; Pfeiffer Vacuum, Thermostar) with a heated quartz capillary locate beneath the catalyst bed. The inlet of the QMS was maintained at an elevated temperature (433 K) to prevent condensation of H_2O vapor that evolved during the reduction of oxidized catalysts.

To obtain each temperature programmed reduction profile, the catalyst was first heated to 573 K in flowing dry air (101 kPa, 100 cm^3 min^{-1}) to ensure the catalyst was fully oxidized and that adsorbed H_2O was removed from the support. At 573 K, the reactor was purged with pure He (101 kPa, 100 cm^3 min^{-1}) and then cooled to near ambient temperature (~303 K). The gas flow was directed through the bypass and then changed to a mixture of H_2 and He (41 kPa H_2, 60 kPa He, 60 cm^3 min^{-1}). While the H_2/He flow and the signal on the QMS stabilized, the catalyst bed was cooled to ~263 K by directing a stream of cold N_2 vapor (~77 K) over the outside of the quartz tube. This step was necessary because Pd oxides are reported to reduce below ambient temperatures (<295 K) [43]. Once the catalyst bed was cooled, the H_2/He mixture was directed through the catalyst bed for 5 min with continued contact with cold N_2 vapor to purge the reactor with H_2 and He and until the signals from the QMS stabilized. Subsequently, the liquid N_2 vapor was stopped and the catalyst bed warmed naturally to 273 K, at which point the furnace was used to heat the sample from 273 K to 573 K at 3 K min^{-1}. During the ramp, the concentration of H_2O (18 m/z) was monitored using the QMS. The consumption of H_2 (2 m/z) from the gas stream was intentionally low during reduction in order to avoid a gradient in the reactor and was too small to accurately quantify with the QMS.

Fig. 3 shows the TPR profiles for all Pd and $PdZn_x$ catalysts used for kinetic measurements. Empty SiO_2 and SiO_2 supported Zn did not evolve H_2O over the temperature range tested (not shown). Pd reduction began at 297 K while reduction of $PdZn_x$ catalysts began between 321 and 349 K. This experiment confirms that 673 K is a high enough temperature to ensure that all the catalysts are reduced (Section 2.1). The shift to higher reduction temperatures after the addition of Zn implies that the Pd and Zn have alloyed together in $PdZn_x$ catalysts. $PdZn_6$ begins to reduce at lower temperatures than $PdZn_{1.5}$ and $PdZn_{30}$, which indicates that this material contains a larger quantity of fcc Pd or fcc PdZn nanoparticles that are more readily reduced than β_1-Pd_1Zn_1 nanoparticles that predominate in $PdZn_{30}$ (Fig. 2 and Section S3).

2.3. Steady-state H_2O_2 and H_2O rate measurements

The experimental set-up and procedure used to measure steady-state formation rates have been described in detail

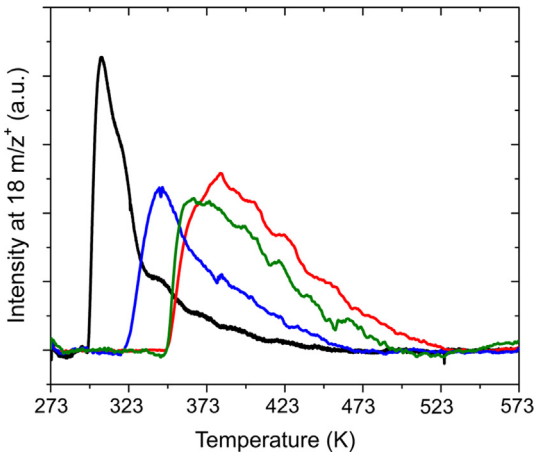

Fig. 3. Temperature programmed reduction profiles for Pd (black), $PdZn_{1.5}$ (red), $PdZn_6$ (blue), and $PdZn_{30}$ (green) catalysts (3 K min^{-1}, 41 kPa H_2, 60 kPa He, 60 cm^3 min^{-1}).

previously [29,30]. Briefly, a stainless-steel reactor (15 cm long, 0.5 cm diameter) equipped with a liquid cooling jacket was loaded with 300–600 mg of catalyst on support particles between 35 and 60 mesh. Certified reactant gas mixtures (25% H_2, balance N_2 and 5% O_2, balance N_2; 5% H_2, balance N_2 and 25% O_2, balance N_2; Airgas), outside of the flammable region for H_2/O_2 mixtures [44], were connected to a gas-handling manifold and introduced to the system using digital MFCs (Porter, 601 series). The gas stream was mixed upstream of the reactor with a 20% v/v aqueous methanol (Macron, ≥99.8%) solution using a high-performance liquid chromatography (HPLC) pump (SSI, M1 class). H_2O_2 hydrogenation rates were measured by adding H_2O_2 (Avantor, 30–32%) to the aqueous methanol solution to achieve 1 mM H_2O_2. The pressure of the system was maintained using a back-pressure regulator (BPR; Equilibar, EB1LF1-SS316) which was controlled with an electronic pressure reducer (Proportion Air, QB1S). The reactor temperature was maintained by flowing a 60% v/v aqueous EG mixture held within a refrigerated recirculating bath (Fisher Scientific, Isotemp) through the liquid cooling jacket of the reactor. The gas was removed from the reactor effluent using a polyvinyl chloride gas-liquid separator and was then separated and analyzed using a gas chromatograph (Agilent, 7890, thermal conductivity detector, Ar carrier and reference gas) equipped with a packed column (Molecular Sieve 5A, 3 m length × 2.1 mm inner diameter). The liquid stream was directed through a 10-port valve (Vici) every 10 min, where a 0.4 cm^3 sample was collected and injected into glass test tubes contained within a fraction collector (Biorad, 2110). The 10-port valve also injected 1 cm^3 of a colorimetric indicator solution (12 mM neocuproine, Sigma-Aldrich, ≥98%; 8.3 mM $CuSO_4$, Fisher Scientific ≥98.6%; 25% v/v ethanol, Decon Laboratories Inc., 100%) [45] into each test tube every 10 min. The light absorbance of the liquid within the test tubes at 454 nm were individually analyzed using a spectrophotometer (Spectronic, 20 Genesys) to measure the concentration of H_2O_2 based off calibration curves created using solutions with known H_2O_2 concentrations.

Formation and hydrogenation rates were measured in the absence of mass transport restrictions (i.e., satisfied the Madon-Boudart criteria [46]). Previous studies have shown that artifacts from mass transport restrictions are satisfied if the Pd loading is kept at 0.05 wt.% Pd or less [30]. The same SiO_2 was used as a support (i.e., same diameter, pore volume, and tortuosity) and all the Pd and $PdZn_x$ catalysts synthesized maintained a Pd loading of 0.05 wt.% or less (Table 1) in this study, therefore, these catalysts will not be affected by mass transport limitations. Additionally, H_2 consumption rates per unit volume of $PdZn_x$ catalysts were less than those on Pd, indicating that the Thiele modulus of $PdZn_x$ catalysts were also equal to or less than one (Supporting Information, Section S1) [47]. Rates were measured near differential conversion (<15%) whenever possible to minimize secondary reactions, however, H_2 conversion reached values as high as 22% on $PdZn_6$ catalysts and 25% on Pd catalysts at the highest temperatures (297–305 K) tested, because the total gas flow was kept constant to avoid changes in sensitivity factors for the thermal conductivity detector. H_2O_2 selectivities vary by less than 4% as H_2 conversions increase from 3% to 32% on Pd-SiO_2 catalysts [29], which shows that secondary reactions are insignificant over the range of H_2 conversions tested. This together, with the greater primary H_2O_2 selectivities and lower H_2O_2 decomposition rates for $PdZn_x$ catalysts, indicate that the few H_2O_2 formation rates not measured at differential conversion will be minimally affected. Note, H_2O_2 hydrogenation ($H_2 + H_2O_2 \rightarrow 2H_2O$) is discussed here as the predominant pathway for H_2O_2 consumption, because hydrogenation rates are significantly greater than rates for H_2O_2 decomposition ($2H_2O_2 \rightarrow 2H_2O + O_2$) over wide ranges of reaction conditions [14,29,48,49].

Rates were normalized by the number of moles of total surface metal atoms (M_s) estimated from the mean diameter and combined metal loading of Pd and Zn (Table 1). Zn is not active for H_2O_2 formation by direct synthesis [21], therefore, Pd surface atoms (Pd_s) likely comprise the active sites for these reactions. The crystal structure of PdZn bimetallic nanoparticles are β_1-Pd_1Zn_1 (Fig. 2), which suggests that roughly one-half of the surface atoms in PdZn alloyed nanoparticles are Zn and that turnover rates on $PdZn_x$ may be greater than reported here by as much as a factor of two. Measurements of the effects of reactant pressures and temperature on primary reaction rates were taken after H_2O_2 and H_2O formation rates became nearly independent of time on stream (e.g., <5% change over 8 h) with the exception of the $PdZn_6$ material, which was less stable than other catalysts examined leading to greater uncertainties particularly in formation rates of H_2O. The catalysts required between 6 and 24 h of continuous reaction to achieve stable rates (Section S5). After this period, linear corrections were used to correct site counts for deactivation during the course of experiments, and uncertainties from those corrections are propagated to reported turnover rates.

2.4. Rate measurements in a semi-batch reactor

H_2O_2 formation rates were measured in protic (methanol) and aprotic (acetonitrile; Avantor, 99.9%; and dimethyl sulfoxide; Macron, 99.9%) solvents in a semi-batch reactor configuration described previously [29]. Briefly, 80 cm^3 of solvent was added to a 100 cm^3 three-neck round bottom flask equipped with a condenser column followed by the introduction of a reactant gas stream (4.2 kPa H_2, 4.2 kPa O_2, 93 kPa N_2) using a variable area rotameter (Omega, FL-1461-S). Next, 200–300 mg of catalyst was added to the flask to initiate the reaction, which proceeded under continuous stirring and at ambient temperature (~295 K). Liquid samples (0.5 cm^3) were collected every 5–30 min with a filtered syringe to prevent contamination of the sample by the catalyst. The H_2O_2 concentration of each liquid sample was determined using the colorimetric titration procedure described above (Section 2.3).

3. Results and discussion

3.1. Steady-state rates and mechanisms for H_2O_2 and H_2O formation

Fig. 4 shows turnover rates for the formation of H_2O_2 (Fig. 4a) and H_2O (Fig. 4b) at steady-state and as a function of H_2 pressure ((H_2)) on Pd, $PdZn_6$, and $PdZn_{30}$ catalysts (40–400 kPa H_2, 60 kPa O_2, 281 K). H_2O_2 formation rates (Fig. 4a) increase approximately linearly with H_2 pressure ($(H_2)^{0.8-1.2}$) below 100 kPa H_2, above which, H_2O_2 rates exhibit a sublinear dependence on H_2 pressure ($(H2)^{0.3-0.5}$) on all three catalysts. H_2O formation rates (Fig. 4b) also increase from 40 to 100 kPa H_2 but do so with a wider range of hydrogen pressure dependencies ($(H_2)^{-0.1-1.3}$). H_2O formation rates do not change significantly with (H_2) values above 100 kPa with the exception of $PdZn_6$ which show a decrease attributed to instability of this material. These dependencies of both H_2O_2 and H_2O formation rates on (H_2) for Pd and $PdZn_x$ catalysts resemble those reported previously for 0.7 nm Pd nanoparticles [30] and for AuPd catalysts 8–10 nm in diameter [29], which suggests that the mechanistic interpretation of these data will lead to similar conclusions. Fig. 5 indicates that turnover rates for the formation of H_2O_2 (Fig. 5a) and H_2O (Fig. 5b) depend only weakly on the (O_2) for Pd, Pd_1Zn_6, and Pd_1Zn_{30} catalysts (50–400 kPa O_2, 60 kPa H_2, 281 K). The independence of rates on (O_2) suggests that active sites predominantly bind O_2-derived reactive intermediates across this range of reactant pressures. Together with the concurrent

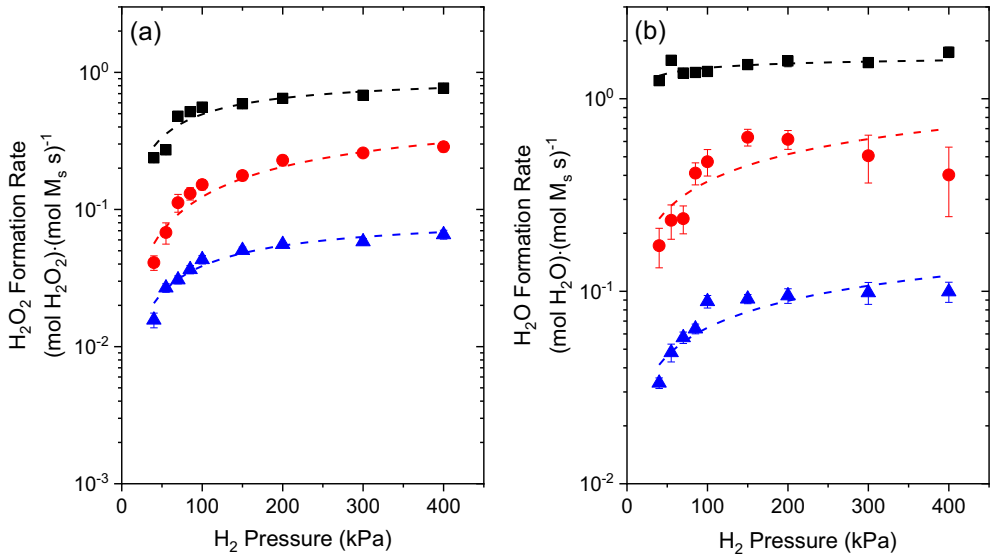

Fig. 4. Turnover rates for the formation of (a) HO_2 a2nd (b) H_2O as functions of H pressure on silica-supported2 Pd (■), $PdZn_6$ (●), and $PdZn_{30}$ (▲) (60 kPa O_2, 281 K, 30 cm^3 min^{-1} 20% v/v methanol). Dashed lines in (a) and (b) represent fits to the forms of the rate equations for H_2O_2 (Eq. (2)) and H_2O (Eq. (5)), respectively.

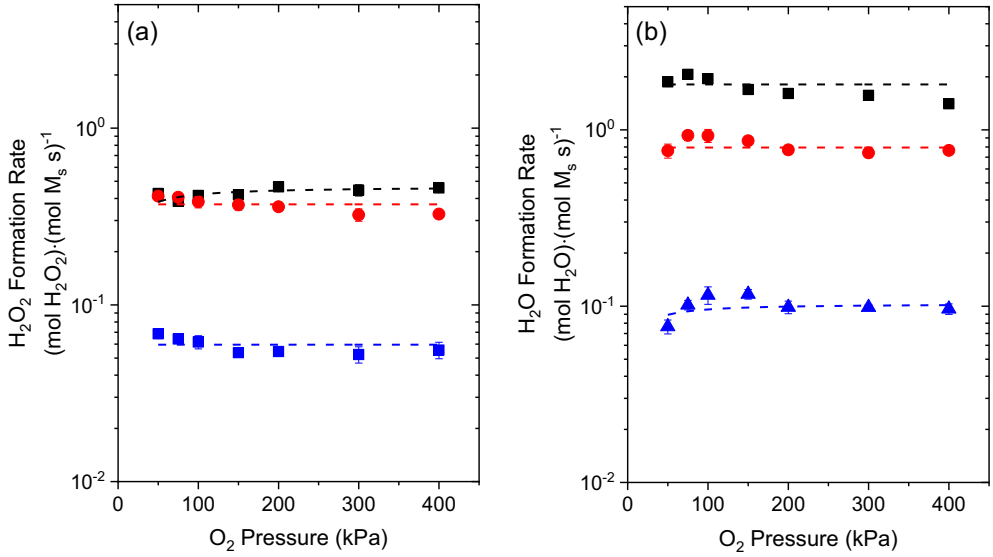

Fig. 5. Turnover rates for the formation of (a) H_2O_2 and (b) H_2O as functions of O_2 pressure on silica-supported Pd (■), $PdZn_6$ (●), and $PdZn_{30}$ (▲) (60 kPa H_2, 281 K, 30 cm^3 min^{-1} 20% v/v methanol). The dashed lines in (a) and (b) show fits to the forms of the rate equations for H_2O_2 (Eq. (2)) and H_2O (Eq. (5)), respectively.

change in the dependence of both H_2O_2 and H_2O formation rates on (H_2) (Fig. 4), these observations would be consistent with a change in the most abundant reactive intermediates (MARI) from O_2^{**} at low values of (H_2) to OOH^{**} species at higher (H_2) [29]. Computational investigations of surface bound O_2 and OOH intermediates indicate these species likely bind to two or more neighboring Pd atoms in η^2 and bent η^1 configurations [50–54], where one O-atom may reside in a three-fold hollow while the other coordinates to a two-fold or atop site. Consequently, we denote these species as O_2^{**} or OOH^{**} to reflect the multidentate coordination of these intermediates to ensembles of metal atoms.

Scheme 1 shows the proposed series of elementary steps for H_2O_2 formation by direct synthesis on transition metal catalysts, whereas, those that produce H_2O are included in Scheme S1. Briefly, H_2 adsorbs dissociatively onto the metal surface (Scheme 1, step 1) followed by heterolytic dissociation of H^*-atoms into protons and electrons (Scheme 1, step 2). Molecular adsorption of O_2 (Scheme 1, step 3) is followed by facile proton-electron transfer (PET) to O_2^{**} that forms OOH^{**} (Scheme 1, step 4). Subsequently, a second, kinetically relevant PET process converts OOH^{**} into $H_2O_2^{**}$ (Scheme 1, step 5). These PET steps likely involve liquid-phase complexes (e.g., H_3O^+, $CH_3OH_2^+$) or adsorbed oxygenate species that shuttle protons, whereas electrons transfer through surface states of Pd and $PdZn_x$ nanoparticles. The $H_2O_2^{**}$ produced desorbs from the surface into the solution (Scheme 1, step 6) to complete the cycle. Although previous reports for H_2O_2 formation on PdZn nanoparticles did not address the reaction mechanism [20,21], the steps proposed here to form H_2O_2 and H_2O agree with previous findings for smaller Pd nanoparticles [30] and AuPd [29] catalysts.

The law of mass action gives the rate for the kinetically relevant elementary step that forms H_2O_2 (r_5, Scheme 1). When combined with the pseudo-steady state hypothesis for the reactive surface intermediates (e.g., $[O_2^{**}]$, $[OOH^{**}]$) and the conservation of the

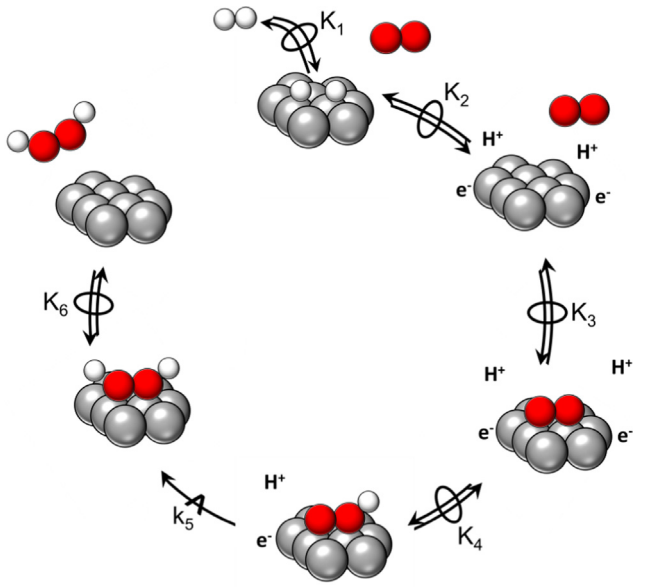

Scheme 1. Proposed elementary steps for H_2O_2 formation by direct synthesis from reactions of O_2 (red spheres) and H_2 (white spheres) derived intermediates on Pd and $PdZn_x$ nanoparticles. Here, ⟷ indicates that an elementary step is quasi-equilibrated, → indicates that an elementary step is kinetically relevant, and k_x and K_x are the rate and equilibrium constants for elementary step x.

total number of active sites, the expression for the turnover rate for H_2O_2 formation takes the form:

$$\frac{r_{H_2O_2}}{[L]} = \frac{k_5 K_4 K_3 K_2{}^2 K_1 (H_2)(O_2)}{1 + K_3(O_2) + K_4 K_3 K_2 K_1{}^{\frac{1}{2}} (H_2)^{\frac{1}{2}} (O_2) + \frac{1}{K_6}(H_2O_2)} \quad (2)$$

where [L] is the total number of sites, (H_2O_2) is the liquid-phase concentration of H_2O_2, and k_x and K_x are the rate and equilibrium constants for elementary steps *x*. The complete derivation is presented within Supporting Information, Section S6 and previous work [30]. The weak dependence of H_2O_2 formation turnover rates on (O2) (Fig. 5a) suggests the MARI contains molecular O_2 (e.g., O_2** or OOH**). If the MARI is O_2**, Eq. (2) simplifies to:

$$\frac{r_{H_2O_2}}{[L]} = k_5 K_4 K_2{}^2 K_1 (H_2) \quad (3)$$

Eq. (3) is qualitatively consistent with measured trends in H_2O_2 over all (O2) values tested (Fig. 5a) and low (H2) values (Fig. 4a, 40–100 kPa H_2) for Pd and $PdZn_x$ catalysts (Section S6). If instead OOH** is the MARI, Eq. (2) becomes:

$$\frac{r_{H_2O_2}}{[L]} = k_5 K_2 K_1{}^{\frac{1}{2}} (H_2)^{\frac{1}{2}} \quad (4)$$

The half-order dependence on (H2) in Eq. (4) is consistent with the sub-linear dependence on (H_2) above 100 kPa H_2 in Fig. 4a, which implies that the MARI changes from O_2** to OOH** at sufficiently high (H_2) values. These H_2O_2 dependencies on (H_2) and (O_2) for $PdZn_x$ catalysts (Figs. 4a and 5a) strongly resemble those for Pd [30] and AuPd [29] which likely form H_2O_2 by PET steps (Scheme 1). The functional form of Eq. (2) accurately describes H_2O_2 formation rates on the three catalysts, as shown by the close agreement between the fit of this expression to measured turnover rates (Figs. 4a and 5a). These comparisons suggest that H_2O_2 formation on $PdZn_x$ catalysts also occurs by PET involving solvent or solvent-derived species and not by direct transfer of H*-atoms from active sites on catalyst nanoparticles to adsorbed dioxygen species.

Reaction pathways that produce H_2O involve processes similar to those for H_2O_2 formation, however, O-O bonds cleave irreversibly [55] in O_2** (Scheme S1, step 7), OOH** (Scheme S1, step 8), and H_2O_2** (Scheme S1, step 12) prior to complete reduction of oxygen and the desorption of H_2O. Intrinsic energy barriers for O-O bond scission in OOH** are significantly lower than in O_2** on Pd(1 1 1) [50,52], so rates of H_2O formation are proposed to be determined by the rate of O-O bond cleavage in OOH** (Scheme S1, step 8) at the conditions studied here. Applying the pseudo-steady state hypothesis to the coverage of reactive species involved in Scheme S1, the rate of step 8 (r_8) cans be restated as a function of equilibrium and rate constants and reactant pressures to describe the primary rate of H_2O formation (r_{H_2O}):

$$\frac{r_{H_2O}}{[L]} = \frac{k_8 K_4 K_3 K_2 K_1{}^{\frac{1}{2}} (H_2)^{\frac{1}{2}} (O_2)}{1 + K_3(O_2) + K_4 K_3 K_2 K_1{}^{\frac{1}{2}} (H_2)^{\frac{1}{2}} (O_2) + \frac{1}{K_6}(H_2O_2)} \quad (5)$$

As described above, if H_2O_2 and H_2O form on the same type of site, the MARI for H_2O formation is O_2** at (H_2) values between 55 and 100 kPa H_2, which simplifies Eq. (5) to the form:

$$\frac{r_{H_2O}}{[L]} = k_8 K_4 K_2 K_1{}^{\frac{1}{2}} (H_2)^{\frac{1}{2}} \quad (6)$$

and for an OOH** MARI (e.g., > 100 kPa H_2), Eq. (5) becomes:

$$\frac{r_{H_2O}}{[L]} = k_8 \quad (7)$$

Qualitative inspection of Eqs. (6) and (7) demonstrate that these expressions match the rate data (Fig. 4b and 5b) over the reactant pressure ranges where O_2** and OOH** are expected to be the MARI, respectively. Moreover, the form of Eq. (5) matches the full range of H_2O formation rate measurements, as by reasonable agreement between the fit lines depicted in Fig. 4b and 5b and the reported turnover rates. Together, these comparisons of Eqs. (2) and (5) to H_2O_2 and H_2O formation rate dependencies on (H_2) and (O_2) strongly suggest that the same mechanisms for H_2O_2 and H_2O formation that occur on those catalysts occur on $PdZn_x$ as well.

Fig. 6 shows H_2O_2 concentration measured as a function of time in a semi-batch reactor containing the $PdZn_{30}$ catalyst (largely β_1-Pd_1Zn_1 nanoparticles with detectable quantities of Pd and Zn oligomers and small (<1 nm) nanoparticles, Figs. 2 and S5) and methanol, acetonitrile, or dimethyl sulfoxide, which are representative of potential protic and aprotic solvents for direct synthesis H_2O_2 forms readily in methanol, and the change in the H_2O_2 concentration as a function of time in methanol follows expectations for the rate of primary H_2O_2 formation at low H_2 pressures (Eq. (3)) and a rate for secondary H_2O_2 hydrogenation that is proportional to the concentration of H_2O_2. Consequently, initial net rates of H_2O_2 formation suggest primary formation of H_2O_2 proceeds with a turnover rate of $(6.6 \pm 0.3)\cdot 10^{-3}$ mol H_2O_2 mol M_s^{-1} s^{-1}. However, H_2O_2 concentrations remain undetectable in acetonitrile and dimethyl sulfoxide over the full course of the experiments (within the uncertainty of the measurement), which suggests that turnover rates for H_2O_2 formation on the same catalyst ($PdZn_{30}$) are at least 100-times lower in acetonitrile and dimethyl sulfoxide. As discussed previously [29,30], detectable H_2O_2 formation rates in protic solvents and undetectable rates in aprotic solvents indicate that proton-electron transfer processes reduce O_2 to H_2O_2 (Scheme 1), because these steps involve lower barriers and occur more readily in protic solutions. This evidence (Fig. 6), combined with the dependence of formation rates on (H_2) and (O_2) (Figs. 4 and 5), strongly suggests that the direct synthesis of H_2O_2 on β_1-Pd_1Zn_1 nanoparticles occurs by the proposed proton-electron transfer mechanism (Scheme 1) and likely does not involve direct addition of chemisorbed H*-atoms to O_2** and OOH**.

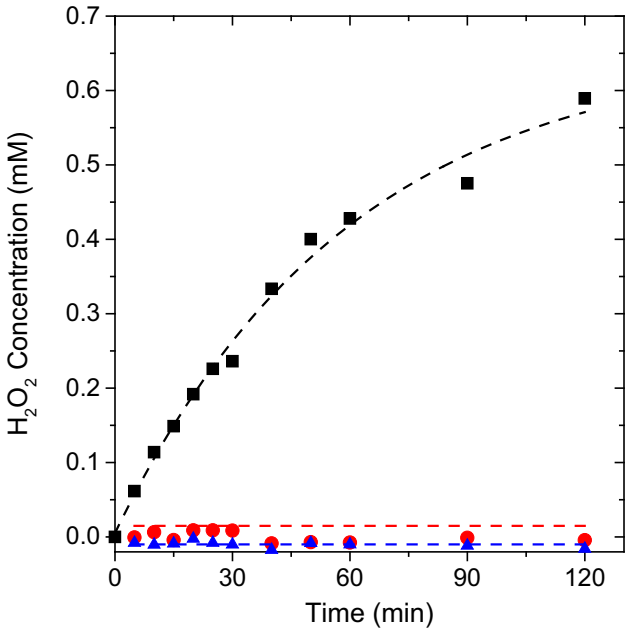

Fig. 6. H_2O_2 concentrations as functions of time during catalysis in a semi-batch reactor on $PdZn_{30}$ in methanol (■), acetonitrile (●), and dimethyl sulfoxide (▲) at 295 K (4.2 kPa H_2, 4.2 kPa O_2, 80 cm^3 solvent). Dashed line represent fits to a model describing primary H_2O_2 formation and secondary H_2O_2 decomposition reactions.

3.2. Effects of adding Zn to Pd on H_2O_2 selectivity, product formation rates, and H_2O_2 hydrogenation rates

Fig. 7 shows H_2O_2 and H_2O formation rates and H_2O_2 selectivity as a function of the bulk Pd:Zn ratio of the catalyst, and these comparisons show that the addition of Zn to Pd decreases H_2O_2 and H_2O formation rates by as much as 20- and 130-fold, respectively (Fig. 7a). The combined differences in these primary reaction rates lead to a concomitant increase in the selective conversion of H_2 to H_2O_2 from 26% on Pd to 69% on $PdZn_{30}$ (Fig. 7b). The changes in rates upon addition of Zn are, however, not monotonic functions of the Pd:Zn ratio. $PdZn_6$ gives higher rates of H_2O_2 and H_2O formation than $PdZn_{1.5}$ (Fig. 7a), while these two catalysts provide H_2O_2 selectivities that equal within the error of the measurements (Fig. 7b). The differences in the rates along with the similar H_2O_2 selectivities are likely a consequence of non-uniformities in the distributions of Pd and β_1-Pd_1Zn_1 nanoparticles within each material, which introduces uncertainty into estimates for the number of active sites and presents distributions of catalytically distinct active sites. Comparisons between X-ray diffraction patterns (Fig. 2) support this interpretation and show that fcc Pd and β_1-Pd_1Zn_1 nanoparticles coexist within these catalysts. Excessive amounts of Zn atoms (i.e., compositions such as $PdZn_{30}$) are needed to convert the majority of Pd nanoparticles into β_1-Pd_1Zn_1. Small quantities of Pd and Zn do not alloy and reside on the support likely in the form of Pd oligomers and nanoparticles (<1 nm) and ZnO deposits, respectively, based upon STEM-EDX analysis (Section S4).

Turnover rates for H_2O_2 hydrogenation on $PdZn_{30}$ are nearly an order of magnitude lower than on Pd (Fig. 8), which suggests that β_1-Pd_1Zn_1 nanoparticles provide greater H_2O_2 selectivities by decreasing rates of secondary reactions that consume H_2O_2 in addition to giving greater primary selectivities within primary reaction pathways. The differences between H_2O_2 hydrogenation rates, however, are less significant than differences between the turnover rates for primary H_2O_2 and H_2O formation (i.e., 20- and 130-fold, respectively, Fig. 7). Consequently, the predominant reason for greater H_2O_2 selectivities on catalysts containing β_1-Pd_1Zn_1 nanoparticles appears to be the difference in primary rates and selectivities and not the suppression of secondary reactions (Fig. 7b). H_2O_2 hydrogenation rates are greater on $PdZn_6$ compared with $PdZn_{1.5}$, which as discussed above, could reflect uncertainties in estimates for the number of active sites and differences in the distribution of fcc Pd or β_1-Pd_1Zn_1 nanoparticles. Overall, the qualitative trends observed for primary and secondary formation rates and H_2O_2 selectivities among Pd and $PdZn_x$ catalysts (Figs. 7 and 8) match reports for the effects of alloying Pd with Au on the direct synthesis of H_2O_2 [13,14,29,56]. Specifically, selectivities to H_2O_2 increase as the average Pd-Pd coordination number decreases as a result of incommensurate changes in the activation enthalpies ($\Delta H^{\ddagger}$) for H_2O_2 and H_2O formation on active sites comprised of Pd atoms [29]. As with Pd and PdAu catalysts [29], the mechanistic similarities between Pd and $PdZn_x$ catalysts (Section 3.1) show that the differences in H_2O_2 selectivities reflect changes in the

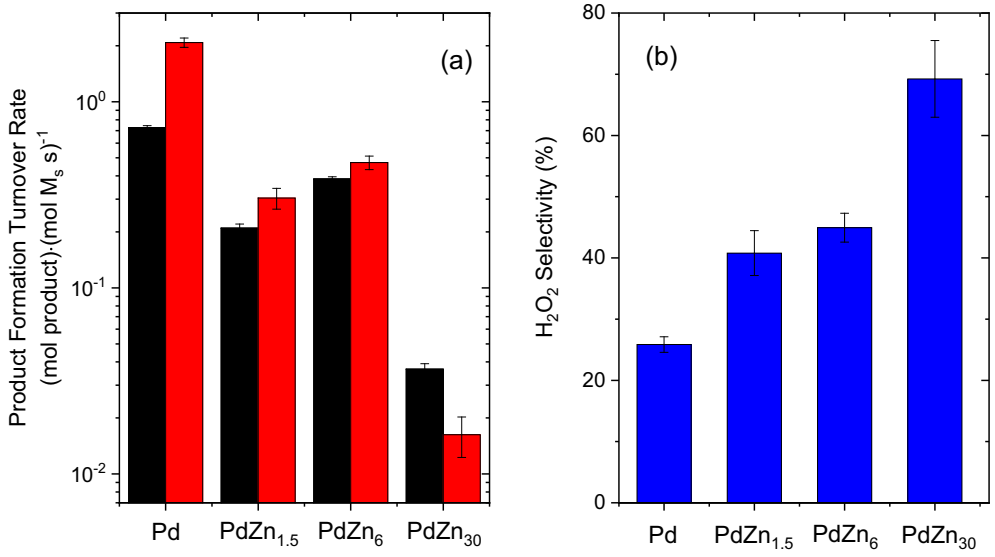

Fig. 7. (a) H_2O_2 (black) and H_2O (red) formation turnover rates and (b) selectivity for the conversion of H_2 into H_2O_2 on different Pd and $PdZn_x$ catalysts (55 kPa H_2, 60 kPa O_2, 273 K, 30 cm^3 min^{-1} 20% v/v methanol).

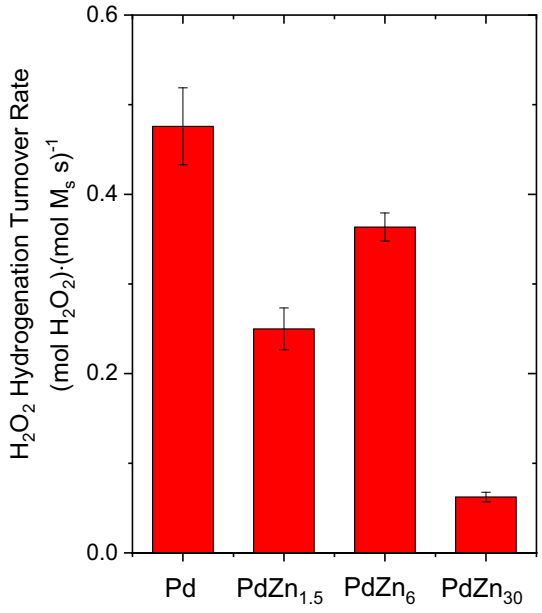

Fig. 8. Turnover rates for H_2O_2 hydrogenation on silica-supported Pd and $PdZn_x$ catalysts (1 mM H_2O_2, 55 kPa H_2, 273 K, 30 cm^3 min^{-1} 20% v/v methanol).

electronic structure of Pd active sites as Pd-Zn bonds replace Pd-Pd coordination during formation of the β_1-Pd_1Zn_1. Correlation of the ratios of turnover rates for primary H_2O_2 formation to those for H_2O to measured $\Delta H^{\ddagger}$ values across the series of Pd and $PdZn_x$ catalysts can reveal independent contributions of electronic and ensemble effects to observed H_2O_2 selectivities on these catalysts that potentially present a number of distinct active sites.

3.3. Activation enthalpies and entropies on Pd and $PdZn_x$ catalysts

Fig. 9 shows H_2O_2 and H_2O formation and H_2O_2 hydrogenation rates on Pd and $PdZn_x$ catalysts as a function of inverse temperature from which values for the $\Delta H^{\ddagger}$ of these reaction pathways were calculated [30]. Briefly, the quasi-equilibrated nature of the elementary steps prior to kinetically relevant H_2O_2 formation (Scheme 1) allow the number of transition states for H_2O_2 formation ($H^+ - OOH**^{\ddagger}$) to be expressed in terms of their equilibrium relationship to gaseous H_2 (H_2(g)) and the MARI (i.e., O_2**):

$$O_2 ** + H_2(g) \overset{K^{\ddagger}_{H_2O_2}}{\leftrightarrow} H^+ - OOH**^{\ddagger} \quad (8)$$

where $K^{\ddagger}_{H_2O_2}$ is the transition state equilibrium constant for the elementary step that forms H_2O_2. Conventions of transition state theory allow the rate of the reaction expressed in Eq. (8) to be stated as:

$$\frac{r_{H_2O_2}}{[L]} = \frac{k_B T}{h} K^{\ddagger}_{H_2O_2}(H_2) \quad (9)$$

in which T is the temperature in Kelvin, and k_B and h are Boltzmann's and Planck's constants, respectively. Similar arguments allow H_2O formation turnover rates to be described via transition state theory as well (Supporting Information, Section S7). Subsequently, the values of $K^{\ddagger}_{H_2O_2}$, which are calculated using measured values of turnover rates and the given (H_2), reflect the difference in Gibb's free energy ($\Delta G^{\ddagger}$) between the product and reactants shown in Eq. (8). Values of the $\Delta H^{\ddagger}$ and the activation entropy ($\Delta S^{\ddagger}$) are determined from the temperature dependence of the $\Delta G^{\ddagger}$ (i.e., from $\Delta G^{\ddagger} = \Delta H^{\ddagger} - T\Delta S^{\ddagger}$).

Table 2 shows $\Delta H^{\ddagger}$ and $\Delta S^{\ddagger}$ values for H_2O_2 ($\Delta H^{\ddagger}_{H_2O_2}$, $\Delta S^{\ddagger}_{H_2O_2}$) and H_2O formation ($\Delta H^{\ddagger}_{H_2O}$, $\Delta S^{\ddagger}_{H_2O}$) and H_2O_2 hydrogenation ($\Delta H^{\ddagger}_{H_2O_2-H}$, $\Delta S^{\ddagger}_{H_2O_2-H}$) calculated from the data in Fig. 9. The values of $\Delta H^{\ddagger}_{H_2O_2}$ for Pd are consistent with prior reports from our group within aqueous methanol solutions (20% by volume methanol in DI water) [29,30] but significantly lower than those for Pd (45 kJ mol^{-1}) [57] and PdAu (44 ± 8 kJ mol^{-1}) [58] within water that contain promoters such as H_2SO_4 and bromide [57], which binds strongly to metal surfaces and likely leads to increases in apparent barriers. Such low $\Delta H^{\ddagger}_{H_2O_2}$ values measured for Pd, $PdZn_{1.5}$, and $PdZn_6$ ($\leq$ 1 kJ mol^{-1}) are similar to reported intrinsic barriers for proton-electron transfer steps measured on Pt electrocatalysts (<15 kJ mol^{-1}) [59] and estimated by DFT (~10 kJ mol^{-1}) [60,61]. Activation enthalpies for all pathways are much lower on Pd nanoparticles than on the $PdZn_{30}$ material, in which Pd exists predominantly within β_1-Pd_1Zn_1 nanoparticles. Notably, values of $\Delta H^{\ddagger}_{H_2O_2}$ and $\Delta H^{\ddagger}_{H_2O}$ on $PdZn_{30}$ are 17 kJ mol^{-1} and 33 kJ mol^{-1} greater than the same barriers on Pd. $\Delta H^{\ddagger}_{H_2O_2}$ and $\Delta H^{\ddagger}_{H_2O}$ values for $PdZn_{1.55}$ and $PdZn_6$ are nearly indistinguishable within the uncertainty of these measurements. The similarity between these $\Delta H^{\ddagger}$ values is consistent with similar H_2O_2 selectivities measured on $PdZn_{1.5}$ and $PdZn_6$ (Fig. 7b) and the proposal that these catalysts have similar fractions of Pd in the form of fcc Pd and β_1-Pd_1Zn_1 nanoparticles (Section 3.2). These comparisons further demonstrate the difficulty in forming ensembles of nanoparticles that consist entirely of β_1-Pd_1Zn_1 because a four-fold change in stoichiometric ratio of Zn to Pd leads to negligible changes in the catalytic behavior of the active sites. The Zn added to the catalysts apparently deposits elsewhere on the surface and does not contribute to reaction pathways that dominate measurements of $\Delta H^{\ddagger}$ on $PdZn_{1.5}$ and $PdZn_6$.

Values of $\Delta H^{\ddagger}$ for primary reactions are much greater for $PdZn_{30}$ ($\Delta H^{\ddagger}_{H_2O_2}$ = 14 kJ mol^{-1}; $\Delta H^{\ddagger}_{H_2O}$ = 44 kJ mol^{-1}), in which Pd atoms primarily reside within β_1-Pd_1Zn_1 nanoparticles. These results combined suggest that alloying Pd with Zn to form β_1-Pd_1Zn_1 phase nanoparticles results in electronic modification of the Pd active sites. These electronic changes most likely result from a narrowing of the d-band center in Pd atoms from intra-atomic orbital hybridization that lead to core-level shifts and cause the d-band center of Pd atoms in PdZn(1 1 1) to be 0.5 eV lower in energy than those in Pd(1 1 1) [32–35,62]. Transition states for O-O bond rupture (i.e., those that form H_2O) are expected to be sensitive to electronic changes of the catalyst surface, because the highest energy electron states on surface Pd atoms must donate multiple electrons to π^* orbitals of the O-O bond to weaken and ultimately cleave this bond. This extent of charge transfer requires significant overlap between the molecular O_2 and surface Pd orbitals, adsorbate structures with O-O bonds nearly parallel to the surface, and thus, the formation of intermediates with stabilities that depend strongly on the d-band structure of the catalyst [50,52,54]. In comparison, proton-electron transfer transition states that form H_2O_2 involve significantly less charge transfer and orbital overlap, compared to those that produce H_2O, and plausibly sense the electronic structure of the catalyst more weakly. Moreover, solvent or solvent-derived molecules that only weakly interact with the catalyst surface also participate in these PET steps. Overall, molecular insight to the reactive species that participate in the kinetically relevant steps for H_2O_2 and H_2O formation and their expected sensitivities to catalyst structure are consistent with values for $\Delta H^{\ddagger}_{H_2O}$ that differ more significantly than for $\Delta H^{\ddagger}_{H_2O_2}$ between Pd and $PdZn_{30}$ catalysts (Table 2).

Values for $\Delta H^{\ddagger}_{H_2O_2-H}$ increase by 8 kJ mol^{-1} between Pd and $PdZn_{30}$ (Table 2) which shows that the formation of β_1-Pd_1Zn_1

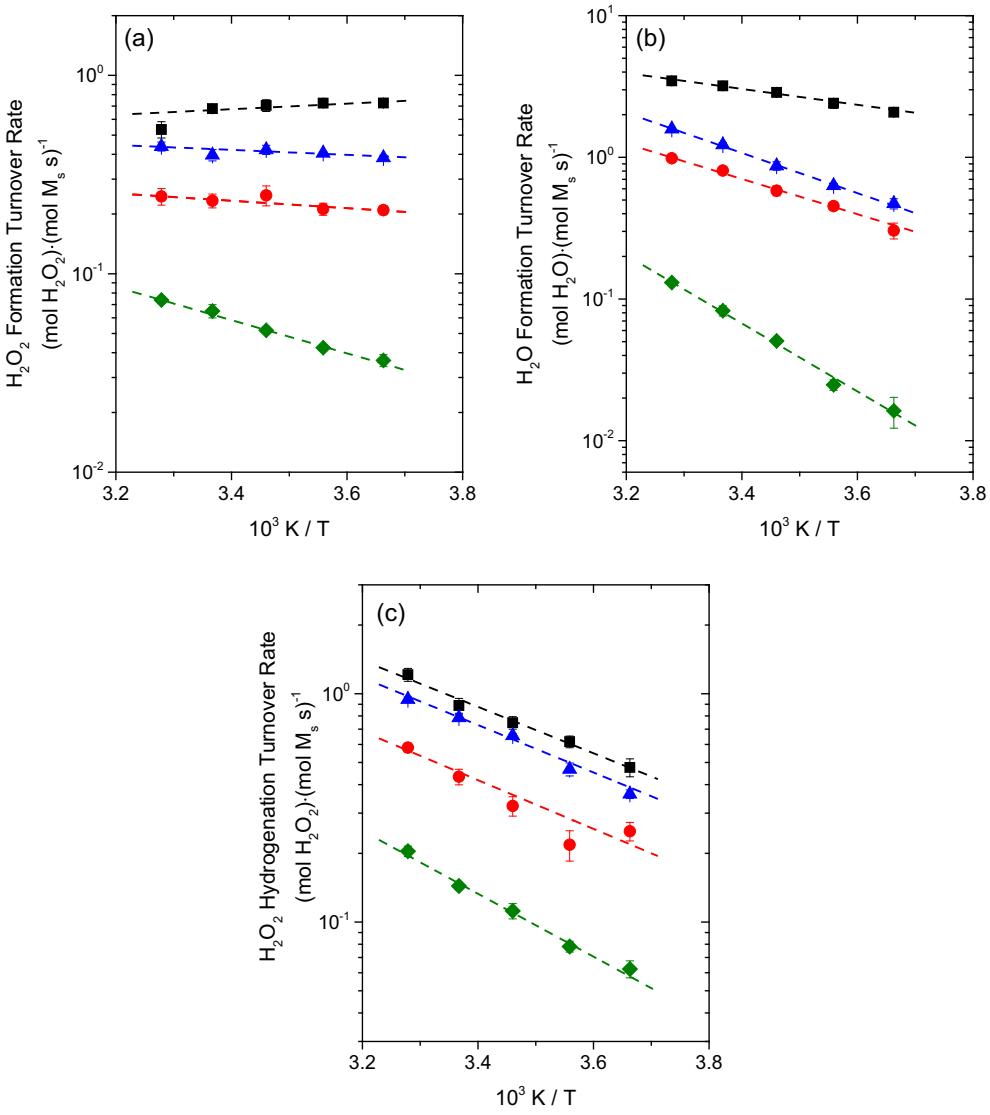

Fig. 9. Turnover rates for the primary formation of (a) H_2O_2 and (b) H_2O as functions of inverse temperature on Pd (■), $PdZn_{1.5}$ (●), $PdZn_6$ (▲), and $PdZn_{30}$ (♦) (55 kPa H_2, 60 kPa O_2, 273–305 K, 30 cm^3 min^{-1} 20% v/v methanol); and for (c) H_2O_2 hydrogenation on the same materials (1 mM H_2O_2, 55 kPa H_2, 273–305 K, 30 cm^3 min^{-1} 20% v/v methanol). Dashed lines represent exponential fits to the data.

Table 2
Activation enthalpies ($\Delta H^{\ddagger}$) and entropies ($\Delta S^{\ddagger}$) for H_2O_2 and H_2O formation and H_2O_2 hydrogenation.[a,b]

Catalyst	$\Delta H^{\ddagger}_{H_2O_2}$ (kJ) (mol)$^{-1}$	$\Delta H^{\ddagger}_{H_2O}$ (kJ) (mol)$^{-1}$	$\Delta H^{\ddagger}_{H_2O_2-H}$ (kJ) (mol)$^{-1}$	$\Delta S^{\ddagger}_{H_2O_2}$ (J) (mol K)$^{-1}$	$\Delta S^{\ddagger}_{H_2O}$(J) (mol K)$^{-1}$	$\Delta S^{\ddagger}_{H_2O_2-H}$ (J) (mol K)$^{-1}$
Pd	−3 ± 1	11 ± 1	18 ± 2	−251 ± 5	−193 ± 3	−185 ± 5
$PdZn_{1.5}$	1 ± 1	21 ± 1	19 ± 3	−247 ± 4	−169 ± 4	−187 ± 10
$PdZn_6$	0 ± 1	25 ± 1	16 ± 1	−246 ± 3	−155 ± 2	−194 ± 5
$PdZn_{30}$	14 ± 1	44 ± 2	26 ± 2	−216 ± 2	−113 ± 6	−175 ± 6

[a] Activation enthalpies and entropies were calculated from Eqs. (9) and (S25) and measured transition state equilibrium constants ($K^{\ddagger}$).
[b] Formation rates were measured at 55 kPa H_2, 60 kPa O_2, 273–305 K, and 30 cm^3 min^{-1} 20% v/v methanol while H_2O_2 hydrogenation rates were measured at 55 kPa H_2, with 30 cm^3 min^{-1} of 1 mM H_2O_2 in 20% v/v methanol, and 273–305 K.

nanoparticles increases barriers for secondary pathways that cleave O—O bonds but do so less effectively than for the primary reactions that form H_2O. The difference in $\Delta H^{\ddagger}_{H_2O_2-H}$ is consistent with H_2O_2 hydrogenation turnover rates that are lower on $PdZn_{30}$ than for other $PdZn_x$ catalysts (Fig. 8). This trend agrees qualitatively with differences between measured $\Delta H^{\ddagger}_{H_2O_2-H}$ values on $PdAu_{12}$ (44 ± 5 kJ mol^{-1}) and on Pd (18 ± 2 kJ mol^{-1}) [29], however, the change in this barrier observed upon alloying Au with Pd is much larger than the 8 kJ mol^{-1} difference between Pd and $PdZn_{30}$. Notably, $\Delta H^{\ddagger}_{H_2O_2-H}$ values were indistinguishable between Pd, $PdZn_{1.5}$, and $PdZn_6$ (16 – 18 kJ mol^{-1}; Table 2).

Measured values for apparent activation enthalpies tend to reflect the barriers for the type of active site that collectively provide the greatest rates for a given pathway across the range of temperatures evaluated. Residual Pd nanoparticles in predominantly bimetallic materials (e.g., PdSn) have been proposed to contribute

significantly to H_2O formation and H_2O_2 hydrogenation rates [20]. Here, $\Delta H^{\ddagger}_{H_2O_2-H}$ values reflect the barriers for this reaction pathway on the residual Pd nanoparticles that exist within $PdZn_{1.5}$ and $PdZn_6$ samples and which are more reactive towards secondary reaction pathways than the β_1-Pd_1Zn_1 bimetallic surfaces [20]. The differences among values of the $\Delta H^{\ddagger}_{H_2O_2-H}$ (10 kJ mol^{-1}) are less than those for $\Delta H^{\ddagger}_{H_2O}$ (33 kJ mol^{-1}) even though the primary and secondary reaction pathways for O—O bond rupture involve similar reactive intermediates and kinetically relevant steps [29,30]. Values for $\Delta H^{\ddagger}_{H_2O_2-H}$ and $\Delta H^{\ddagger}_{H_2O}$ were more comparable to each other on each Pd and $PdAu_x$ catalyst previously reported [29], and the disparities between these barriers among Pd and $PdZn_x$ catalysts imply that two or more distinct active sites exist on $PdZn_x$ nanoparticles and that these sites differ in their contributions to primary rates of H_2O_2 and H_2O formation as well as to secondary H_2O_2 hydrogenation. Simple comparisons between the differences between values of $\Delta H^{\ddagger}_{H_2O}$ and $\Delta H^{\ddagger}_{H_2O_2}$ for Pd and $PdZn_x$ catalysts suggest that H_2O_2 selectivities should increase significantly more than observed (i.e., 26% on Pd to 69% on $PdZn_{30}$) if all catalytically active sites are equivalent within each material. These conclusions are supported also by the systematic change in the difference between activation entropies for H_2O_2 and H_2O formation pathways ($\Delta\Delta S^{\ddagger} = \Delta S^{\ddagger}_{H_2O_2} - \Delta S^{\ddagger}_{H_2O}$). Conceptually, values of $\Delta\Delta S^{\ddagger}$ should remain constant when a series of catalysts facilitate a reaction through identical mechanisms, as shown for H_2O_2 and H_2O formation on Pd and $PdZn_x$. $\Delta\Delta S^{\ddagger}$ decreases systematically (e.g., from −58 J mol^{-1} K^{-1} for Pd to −103 J mol^{-1} K^{-1} for $PdZn_{30}$; Table 2), however, which suggests that addition of Zn leads to heterogeneities among active sites on a given material and that these changes appear as inaccuracies in estimates for site counts used to calculate turnover rates and $\Delta S^{\ddagger}$.

Additional, inequivalent active sites may be revealed by comparisons of the ratios of turnover rates (normalized by estimates for the number of active sites) to differences in $\Delta H^{\ddagger}$ for parallel reaction pathways. Changes in $\Delta H^{\ddagger}_{H_2O_2}$ and $\Delta H^{\ddagger}_{H_2O}$ values indicate that H_2O_2 selectivities should increase when Zn alloys with Pd, at least in part, as a result of changes in the electronic structure of the active sites. H_2O_2 selectivities can be expressed as the ratio of product formation rates defined as χ:

$$\chi = \frac{\left(\frac{r_{H_2O_2}}{[L]}\right)}{\left(\frac{r_{H_2O}}{[L']}\right)} \tag{10}$$

Eq. (10) can be reformulated as a function of the difference in activation enthalpies for H_2O_2 and H_2O formation ($\Delta\Delta H^{\ddagger} = \Delta H^{\ddagger}_{H_2O_2} - \Delta H^{\ddagger}_{H_2O}$) by proposing that both reactions occur on the same set of active sites (i.e., [L] equals [L′]), using the relevant forms of the turnover rate expressions for H_2O_2 (Eq. (9)) and H_2O (Eq. S25), and expressing free energy changes in terms of the contributions of enthalpy and entropy (i.e., $\Delta G^{\ddagger} = \Delta H^{\ddagger} - T\Delta S^{\ddagger}$):

$$\chi = (H_2)^{\frac{1}{2}} \cdot \left(e^{\frac{-\Delta\Delta H^{\ddagger}}{RT}}\right) \cdot \left(e^{\frac{\Delta\Delta S^{\ddagger}}{R}}\right) \tag{11}$$

where R is the ideal gas constant. Values of $\Delta\Delta H^{\ddagger}$ do not depend on active site counts and are calculated from values in Table 2. If all active sites are catalytically equivalent within a given material, then the number of active sites for H_2O_2 and H_2O formation are equal. Similarly, if the mechanism for the reaction does not change with the composition of the catalyst, then the true values of $\Delta\Delta S^{\ddagger}$ and the dependence on (H_2) remain constant among a series of materials (i.e., Pd and $PdZn_x$). In these cases, the H_2O_2 selectivity, expressed as χ, will be a single value function of terms $\Delta\Delta H^{\ddagger}/T$. These assumptions can be tested by inspecting plots of measured χ values as functions of $\Delta\Delta H^{\ddagger}/T$, because differences from the expected behavior provides a direct method to catalytically detect inequivalent active sites whose presence may evade structural characterization.

Fig. 10 shows that χ values increase with the bulk ratio of Zn to Pd across the series of Pd and $PdZn_x$ catalysts. However, the simple model described by Eq. (11) predicts that significant difference between $\Delta\Delta H^{\ddagger}$ for Pd and for $PdZn_{30}$ (16 kJ mol^{-1}; Table 2) should give a value of χ that is three- to four-orders of magnitude greater on $PdZn_{30}$ than on Pd, when each catalyst contains a single type of active site and activation entropy differences remain constant at equivalent conditions (55 kPa H_2, 60 kPa O_2, 273–305 K). The changes in χ values predicted for $PdZn_x$ catalysts from ideal electronic effects (i.e., when only $\Delta\Delta H^{\ddagger}$values differ between catalysts, Eq. (11)) are depicted by exponential fits within Fig. 10. Comparisons of χ values for $PdZn_{1.5}$, $PdZn_6$, and $PdZn_{30}$ catalysts to those anticipated at a given value of $\Delta\Delta H^{\ddagger}/T$ show that H_2O_2 selectivities are much lower than anticipated from the significant electronic changes to the Pd active sites. The fact that χ values increase modestly (by a factor of 10) and will possess multiple values at a given $\Delta\Delta H^{\ddagger}/T$ for this series of catalysts strongly suggests that at least two catalytically distinct types of sites exist within these materials, of which one type of site preferentially forms H_2O. These non-selective sites partially offset the gains in H_2O_2 selectivities from the electronic differences between Pd active sites in monometallic Pd nanoparticles and those present likely in β_1-Pd_1Zn_1 nanoparticles.

The catalytic sites that lead to H_2O_2 selectivities that are lower than expected (i.e., low χ values in Fig. 10) seem likely to be associated with the small quantities of unalloyed Pd that are detected on the silica support of the $PdZn_{30}$ material by EDX analysis (Fig. S5). Although, stray Zn is also detected, H_2O_2 consumption rates are immeasurable over periods of many hours on catalysts comprised of Zn deposited on SiO_2 (1.4 mM H_2O_2, 60 kPa H_2, 41 kPa He, methanol, 298 K), which suggests that Zn and ZnO do

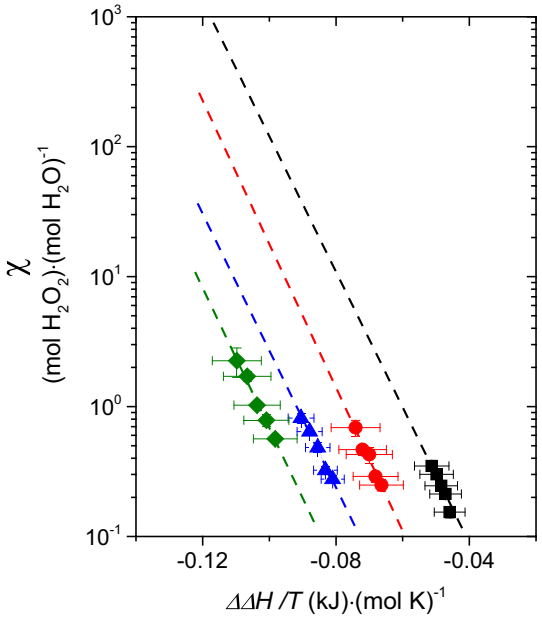

Fig. 10. Ratio of the formation rate of H_2O_2 to that for H_2O (χ) as a function of $\Delta\Delta H^{\ddagger}/T$ on Pd (■), $PdZn_{1.5}$ (●), $PdZn_6$ (▲), and $PdZn_{30}$ (♦) (55 kPa H_2, 60 kPa O_2, 30 cm^3 min^{-1} 20% v/v methanol, 273–305 K). Dashed lines represent exponential fits to measured χ values, and the vertical offsets between fits for Pd and those for $PdZn_x$ materials depict H_2O_2 selectivity losses from the presence of inequivalent sites, which happen to be less selective towards H_2O_2 formation.

not contribute to H_2O_2 hydrogenation. Importantly, these results suggest that much greater H_2O_2 selectivities (e.g., in excess of 99%) might be achieved if precise synthesis methods can be used to form exclusively Pd-Zn intermetallic structures and avoid the deposition of individual, monometallic components on the support, and the formation of monometallic Pd nanoparticles, in particular.

4. Conclusions

H_2O_2 and H_2O formation rates, measured as a function of H_2 and O_2 pressures and temperature on Pd and $PdZn_x$ catalysts, are described by a series of elementary steps that involves proton-electron transfer to O_2^{**} and OOH^{**} intermediates to form H_2O_2 and O-O bond scission to form $H_2O{\cdot}H_2O_2$ formation requires protic solvents and does not proceed at measurable rates in aprotic solvents (e.g., acetonitrile, dimethyl sulfoxide), which demonstrates further that the mechanism for H_2O_2 formation remains constant among Pd, $PdZn_x$, and $PdAu_x$ (previously reported) catalysts. Rates for the formation of H_2O_2 and H_2O as well as the hydrogenation of H_2O_2 (i.e., the desired and undesired pathways and secondary decomposition, respectively) are lower on $PdZn_{30}$ (nearly phase-pure β_1-Pd_1Zn_1) compared to Pd by factors of 20, 130, and 5, respectively. These collective differences lead to H_2O_2 selectivities that are nearly three-fold greater on the most Zn-rich materials. Activation enthalpies ($\Delta H^{\ddagger}$) for H_2O_2 and H_2O formation and H_2O_2 hydrogenation increase with the mole fraction of Zn, where the catalysts that contained primarily β_1-Pd_1Zn_1, and nearly undetectable amounts of Pd, yielded the highest ($\Delta H^{\ddagger}$) for all reaction pathways. Comparisons of the differences between activation enthalpies ($\Delta\Delta H^{\ddagger}$) for the two formation pathways (i.e., H_2O_2 and H_2O) to ratios of the primary rates of formation for H_2O_2 to that of H_2O across Pd and three $PdZn_x$ materials exhibit trends that demonstrate the increase in H_2O_2 results from electronic changes in of Pd active sites caused by alloying with Zn. Yet, H_2O_2 selectivities on the most Zn rich catalyst ($PdZn_{30}$) remain lower than predicted by a simple one-site model analysis of measured rates, which reveals the presence of distinct catalytic sites that preferentially form H_2O and reduce selectivities. These deleterious sites likely consist of small nanoparticles (<1 nm) or oligomers of Pd that are undetectable by XRD and exist near the detection limit for EDX analysis. These findings demonstrate that formation of intermetallic PdZn structures induces electronic changes at the active sites for O_2 reduction that significantly favor the formation of H_2O_2, however, small amounts of Pd that do not alloy significantly reduce selectivities due to their significantly greater dispersion and higher turnover rates. Consequently, increasingly selective catalysts for the direct synthesis of H_2O_2 may be created when the synthesis method ensures that the complete Pd content alloys.

Acknowledgements

Financial support for this work was provided by a research grant from the National Science Foundation (CBET-15531377) and a departmental graduate student fellowship funded by the Dow Chemical Company. This work was carried out in part in the Frederick Seitz Materials Research Laboratory Central Research Facilities, University of Illinois.

Appendix A. Supplementary material

Supplementary data to this article can be found online at https://doi.org/10.1016/j.jcat.2018.09.020.

References

[1] C. Samanta, Direct synthesis of hydrogen peroxide from hydrogen and oxygen: An overview of recent developments in the process, Appl. Catal., A 350 (2008) 133–149.
[2] G. Goor, J. Glennberg, S. Jacobi, Hydrogen peroxide, ullmann's encyclopedia of industrial, Chemistry 18 (2012) 394–427.
[3] G. Blanco-Brieva, M.C. Capel-Sanchez, M.P. de Frutos, A. Padilla-Polo, J.M. Campos-Martin, J.L.G. Fierro, New two-step process for propene oxide production (HPPO) based on the direct synthesis of hydrogen peroxide, Ind. Eng. Chem. Res. 47 (2008) 8011–8015.
[4] V. Russo, R. Tesser, E. Santacesaria, M. Di Serio, Chemical and technical aspects of propene oxide production via hydrogen peroxide (HPPO Process), Ind. Eng. Chem. Res. 52 (2013) 1168–1178.
[5] P. Bassler, H.G. Göbbel, M. Weidenbach, The new HPPO process for propylene oxide: From joint development to worldscale production, Chem. Eng. Trans. 21 (2010) 571–576.
[6] J.M. Campos-Martin, G.B. Blanco-Brieva, J.L.G. Fierro, Hydrogen peroxide synthesis: An outlook beyond the anthraquinone process, Angew. Chem. Int. Ed. 45 (2006) 6962–6984.
[7] A. Tullo, BASF dow plan more propylene oxide units, C&E News 83 (2005) 7.
[8] M. Hey, Paper bleaching: its simple chemistry and working procedures, Paper Conservator 2 (1977) 10–23.
[9] W.H. Glaze, Water, 6, Treatment by Oxidation Processes, Wiley-VCH, Weinheim, Germany, 2011.
[10] O. Tünay, I. Kabdaşı, I. Arslan-Alaton, T. Ölmez-Hanı, Chemical Oxidation Applications for Industrial Wastewaters, IWA Publishing, London, UK, 2010.
[11] J. Garcia-Serna, T. Moreno, P. Biasi, M.J. Cocero, J.-P. Mikkola, T.O. Salmi, Engineering in direct synthesis of hydrogen peroxide: targets, reactors and guidelines for operational conditions, Green Chem. 16 (2014) 2320–2343.
[12] V.R. Choudhary, C. Samanta, Role of chloride or bromide anions and protons for promoting the selective oxidation of H_2 by O_2 to H_2O_2 over supported Pd catalysts in an aqueous medium, J. Catal. 238 (2006) 28–38.
[13] N.E. Ntainjua, M. Piccinini, J.C. Pritchard, J.K. Edwards, A.F. Carley, J.A. Moulijn, G.J. Hutchings, Effect of halide and acid additives on the direct synthesis of hydrogen peroxide using supported gold-palladium catalysts, ChemSusChem 2 (2009) 575–580.
[14] L. Ouyang, G. Da, P. Tian, T. Chen, G. Liang, J. Xu, Y.-F. Han, Insight into active sites of Pd-Au/TiO_2 catalysts in hydrogen peroxide synthesis directly from H_2 and O_2, J. Catal. 311 (2014) 129–136.
[15] G. Käbisch, H. Wittmann, Production of Hydrogen Peroxide by the Anthraquinone Process, United States, 1970.
[16] D.W. Flaherty, Direct synthesis of H_2O_2 from H_2 and O_2 on Pd catalysts: Current understanding outstanding questions, and research needs, ACS Catal. 8 (2018) 1520–1527.
[17] P. Landon, P.J. Collier, A.F. Carley, D. Chadwick, A.J. Papworth, A. Burrows, C.J. Kiely, G.J. Hutchings, Direct synthesis of hydrogen peroxide from H_2 and O_2 using Pd and Au catalysts, Phys. Chem. Chem. Phys 5 (2003) 1917–1923.
[18] J.K. Edwards, A.F. Carley, A.A. Herzig, C.J. Kiely, G.J. Hutchings, Direct synthesis of hydrogen peroxide from H_2 and O_2 using supported Au-Pd catalysts, Faraday Discuss. 138 (2008) 225–239.
[19] P. Biasi, F. Menegazzo, F. Pinna, K. Eränen, T.O. Salmi, P. Canu, Continuous H_2O_2 direct synthesis over PdAu catalysts, Chem. Eng. J. 176–177 (2011) 172–177.
[20] S.J. Freakley, Q. He, J.H. Harrhy, L. Lu, D.A. Crole, D.J. Morgan, E.N. Ntainjua, J.K. Edwards, A.F. Carley, A.Y. Borisevich, C.J. Kiely, G.J. Hutchings, Palladium-tin catalysts for the direct synthesis of H_2O_2 with high selectivity, Science 351 (2016) 965–968.
[21] S. Wang, K. Gao, W. Li, J. Zhang, Effect of Zn addition on the direct synthesis of hydrogen peroxide over supported palladium catalysts, Appl. Catal. A 531 (2017) 89–95.
[22] S. Sterchele, P. Biasi, P. Centomo, P. Canton, S. Campestrini, T. Salmi, M. Zecca, Pd-Au and Pd-Pt catalysts for the direct synthesis of hydrogen peroxide in absence of selectivity enhancers, App. Catal. A 468 (2013) 160–174.
[23] Q. Liu, J.C. Bauer, R.E. Schaak, J.H. Lunsford, Direct synthesis of H_2O_2 from H_2 and O_2 over Pd-Pt/SiO_2 bimetallic catalysts in a H_2SO_4/ethanol system, Appl. Catal., A 339 (2008) 130–136.
[24] V.V. Krishnan, A.G. Dokoutchaev, M.E. Thompson, Direct production of hydrogen peroxide with palladium supported on phosphate viologen phosphonate catalysts, J. Catal. 196 (2000) 366–374.
[25] Q. Liu, J.H. Lunsford, Controlling factors in the direct formation of H_2O_2 from H_2 and O_2 over a Pd/SiO_2 catalyst in ethanol, Appl. Catal., A 314 (2006) 94–100.
[26] S. Chinta, J.H. Lunsford, A mechanistic study of H_2O_2 and H_2O formation from H_2 and O_2 catalyzed by palladium in an aqueous medium, J. Catal. 225 (2004) 249–255.
[27] V.R. Choudhary, Y.V. Ingole, C. Samanta, P. Jana, Direct oxidation of hydrogen to hydrogen peroxide over Pd (or PdO)/Al_2O_3 in aqueous reaction medium: influence of different acids and halide anions in reaction medium on formation and destruction of H_2O_2, Ind. Eng. Chem. Res. 46 (2007) 8566–8573.
[28] J.K. Edwards, A. Thomas, A.F. Carley, A.A. Herzing, C.J. Kiely, G.J. Hutchings, Au-Pd supported nanocrystals as catalysts for the direct synthesis of hydrogen peroxide from H_2 and O_2, Green Chem. 10 (2008) 388–394.
[29] N.M. Wilson, P. Priyadarshini, S. Kunz, D.W. Flaherty, Direct synthesis of H_2O_2 on Pd and Au_xPd_1 clusters: Understanding the effects of alloying Pd with Au, J. Catal. 357 (2018) 163–175.

[30] N.M. Wilson, D.W. Flaherty, Mechanism for the direct synthesis of H_2O_2 on Pd clusters: Heterolytic reaction pathways at the liquid-solid interface, J. Am. Chem. Soc. 138 (2016) 574–586.
[31] N.M. Wilson, Y.T. Pan, Y.T. Shao, J.M. Zuo, H. Yang, D.W. Flaherty, Direct synthesis of H_2O_2 on AgPt Octahedra: The importance of Pt-Ag interactions for high H_2O_2 selectivities, ACS Catal. 8 (2018) 2880–2889.
[32] A. Bayer, K. Flechtner, R. Denecke, H.-P. Steinruck, K.M. Neyman, N. Rosch, Electronic properties of thin Zn layers on Pd(111) during growth and alloying, Surf. Sci. 600 (2006) 78–94.
[33] Z.-X. Chen, K.M. Neyman, A.B. Gordienko, N. Rosch, Surface structure and stability of PdZn and PtZn alloys: Density-functional slab model studies, Phys. Rev. B 68 (2003) 075417.
[34] I. Kovacs, J. Kiss, F. Solymosi, The adsorption properties of $PdZn_x$ alloy on Pd (100): Preparation and characterization, Vacuum 82 (2008) 182–185.
[35] J.A. Rodriguez, Interactions in bimetallic bonding: electronic and chemical properties of PdZn surfaces, J. Phys. Chem. 98 (1994) 5758–5764.
[36] H. Wang, Z. Liu, Y. Ma, K. Julian, S. Ji, V. Linkov, R. Wang, Synthesis of carbon-supported PdSn-SnO_2 nanoparticles with different degrees of interfacial contact and enhanced catalytic activities for formic acid oxidation, Phys. Chem. Chem. Phys 15 (2013) 13999–14005.
[37] L. Jiao, J.R. Regalbuto, The synthesis of highly dispersed noble and base metals on silica via strong electrostatic adsorption: I. Amorhous silica, J. Catal. 260 (2008) 329–341.
[38] R.V. Hardeveld, F. Hartog, The statistics of surface atoms and surface sites on metal catalysts, Surf. Sci. 15 (1969) 189–230.
[39] R.S. Johnson, A. DeLaRiva, V. Ashbacher, B. Halevi, C.J. Villanueva, G.K. Smith, S. Lin, A.K. Datye, H. Guo, The CO oxidation mechanism and reactivity on PdZn alloys, Phys. Chem. Chem. Phys. 15 (2013) 7768.
[40] H. Xiong, A. DeLaRiva, Y. Wang, A.K. Datye, Low-temperature aqueous-phase reforming of ethanol on bimetallic Pd-Zn catalysts, Catal. Sci. Technol. 5 (2015) 254–263.
[41] A. Karim, T. Conant, A. Datye, The role of PdZn alloy formation and particle size on the selectivity for steam reforming of methanol, J. Catal. 243 (2006) 420–427.
[42] Z.-X. Chen, K.M. Neyman, N. Rösch, Theoretical study of segregation of Zn and Pd in Pd-Zn alloys, Surf. Sci. 548 (2004) 291–300.
[43] C.-W. Chou, S.-J. Chu, H.-J. Chiang, C.-Y. Huang, C.-J. Lee, S.-R. Sheen, T.-P. Perng, C.-T. Yeh, Temperature-programmed reduction study on calcination of nano-palladium, J. Phys. Chem. B 105 (2001) 9113–9117.
[44] Safety Standard for Hydrogen and Hydrogen Systems, Guidelines for Hydrogen System Design, Materials Selection, Operations, Storage, and Transportation, National Aeronautics and Space Administration, United States, 1997.
[45] A.N. Baga, G.R.A. Johnson, N.B. Nazhat, R.A. Saadalla-Nazhat, A simple spectrophotometric determination of hydrogen peroxide at low concentrations in aqueous solution, Anal. Chim. Acta 204 (1988) 349–353.
[46] R.J. Madon, M. Boudart, Experimental criterion for the absence of artifacts in the measurement of rates of heterogeneous catalytic reactions, Ind. Eng. Chem. Fundam. 21 (1982) 438–447.
[47] P.B. Weisz, C.D. Prater, Interpretation of measurements in experimental catalysis, Adv. Catal. 6 (1954) 143–196.
[48] S. Melada, R. Rioda, F. Menegazzo, F. Pinna, G. Strukul, Direct synthesis of hydrogen peroxide on zirconia-supported catalysts under mild conditions, J. Catal. 239 (2006) 422–430.
[49] V.R. Choudhary, C. Samanta, P. Jana, Decomposition and/or hydrogenation of hydrogen peroxide over Pd/Al_2O_3 catalyst in aqueous medium: Factors affecting the rate of H_2O_2 destruction in presence of hydrogen, Appl. Catal. A 332 (2007) 70–78.
[50] A. Plauck, E.E. Strangland, J.A. Dumesic, M. Mavrikakis, Active sites and mechanisms for H_2O_2 decomposition over Pd catalysts, Proc. Natl. Acad. Sci. 113 (2016) E1973–E1982.
[51] C.A. Farberow, A. Godinez-Garcia, G. Peng, J.F. Perez-Robles, O. Solorza-Feria, M. Mavrikakis, Mechanistic studies of oxygen reduction by hydrogen on PdAg (110), ACS Catal. 3 (2013) 1622–1632.
[52] D.C. Ford, A.U. Nilekar, Y. Xu, M. Mavrikakis, Partial and complete reduction of O_2 by hydrogen on transition metal surfaces, Surf. Sci. 604 (2010) 1565–1575.
[53] R. Todorovic, R.J. Meyer, A comparative density functional theory study of the direct synthesis of H_2O_2 on Pd Pt and Au surfaces, Catal. Today 160 (2011) 242–248.
[54] W.-Y. Yu, L. Zhang, G.M. Mullen, G. Henkelman, C.B. Mullins, Oxygen activation and reaction on Pd−Au bimetallic surfaces, J. Phys. Chem. C 119 (2015) 11754–11762.
[55] D.P. Dissanayake, J.H. Lunsford, The direct formation of H_2O_2 from H_2 and O_2 over colloidal palladium, J. Catal. 214 (2003) 113–120.
[56] Y.-F. Han, Z. Zhong, K. Ramesh, F. Chen, L. Chen, T. White, Q. Tay, S.N. Yaakub, Z. Wang, Au promotional effects on the synthesis of H_2O_2 directly from H_2 and O_2 on supported Pd-Au alloy catalysts, J. Phys. Chem. C 111 (2007) 8410–8413.
[57] Y. Voloshin, A. Lawal, Kinetics of hydrogen peroxide reduction by hydrogen in a microreactor, Appl. Catal. A 353 (2009) 9–16.
[58] V. Paunovic, J.C. Schouten, T.A. Nijhuis, Direct synthesis of hydrogen peroxide using concentrated H_2 and O_2 mixtures in a wall-coated microchannel – kinetic study, Appl. Catal. A 505 (2015) 249–259.
[59] A.B. Anderson, J. Roques, S. Mukerjee, V.S. Murthi, N.M. Marković, V. Stamenkovic, Activation energies for oxygen reduction on platinum alloys: Theory and experiment, J. Phys. Chem. B 109 (2005) 1198–1203.
[60] M.J. Janik, C.D. Taylor, M. Neurock, First-principles analysis of the initial electroreduction steps of oxygen over Pt(111), J. Electrochem. Soc. 156 (2009) B126–B135.
[61] L. Ou, F. Yang, Y. Liu, S. Chen, First-principle study of the adsorption and dissociation of O_2 on Pt(111) in acidic media, J. Phys. Chem. C 113 (2009) 20657–20665.
[62] B. Halevi, E.J. Peterson, A. DeLaRiva, E. Jeroro, V.M. Lebarbier, Y. Wang, J.M. Vohs, B. Kiefer, E. Kunkes, M. Havecker, M. Behrens, R. Schlogl, A.K. Datye, Aerosol-derived bimetallic alloy powders: bridging the gap, J. Phys. Chem. C 114 (2010) 17181–17190.